

# **SAND REPORT**

SAND2002-1319

Unlimited Release

Printed June 2002

## **Numerical Predictions and Experimental Results of Air Flow in a Smooth Quarter-Scale Nacelle**

Amalia R. Black, Jill M. Suo-Anttila, Louis A. Gritz, Peter J. Disimile, and James R. Tucker

Prepared by  
Sandia National Laboratories  
Albuquerque, New Mexico 87185 and Livermore, California 94550

Sandia is a multiprogram laboratory operated by Sandia Corporation, a Lockheed Martin Company, for the United States Department of Energy under Contract DE-AC04-94AL85000.

Approved for public release; further dissemination unlimited.



**Sandia National Laboratories**

Issued by Sandia National Laboratories, operated for the United States Department of Energy by Sandia Corporation.

**NOTICE:** This report was prepared as an account of work sponsored by an agency of the United States Government. Neither the United States Government, nor any agency thereof, nor any of their employees, nor any of their contractors, subcontractors, or their employees, make any warranty, express or implied, or assume any legal liability or responsibility for the accuracy, completeness, or usefulness of any information, apparatus, product, or process disclosed, or represent that its use would not infringe privately owned rights. Reference herein to any specific commercial product, process, or service by trade name, trademark, manufacturer, or otherwise, does not necessarily constitute or imply its endorsement, recommendation, or favoring by the United States Government, any agency thereof, or any of their contractors or subcontractors. The views and opinions expressed herein do not necessarily state or reflect those of the United States Government, any agency thereof, or any of their contractors.

Printed in the United States of America. This report has been reproduced directly from the best available copy.

Available to DOE and DOE contractors from

U.S. Department of Energy  
Office of Scientific and Technical Information  
P.O. Box 62  
Oak Ridge, TN 37831

Telephone: (865)576-8401  
Facsimile: (865)576-5728  
E-Mail: [reports@adonis.osti.gov](mailto:reports@adonis.osti.gov)  
Online ordering: <http://www.doe.gov/bridge>

Available to the public from

U.S. Department of Commerce  
National Technical Information Service  
5285 Port Royal Rd  
Springfield, VA 22161

Telephone: (800)553-6847  
Facsimile: (703)605-6900  
E-Mail: [orders@ntis.fedworld.gov](mailto:orders@ntis.fedworld.gov)  
Online order: <http://www.ntis.gov/ordering.htm>



SAND2002-1319  
Unlimited Release  
Printed June 2002

## **Numerical Predictions and Experimental Results of Air Flow in a Smooth Quarter-Scale Nacelle**

Amalia R. Black  
Validation and Uncertainty Quantification Processes

Jill M. Suo-Anttila  
Fire Science and Technology

Louis A. Gritzko  
Fire Science and Technology

Sandia National Laboratories  
P.O. Box 5800  
Albuquerque, New Mexico 87185-0828

Peter J. Disimile  
USAF 46 Test Wing Aerospace Survivability and Safety Flight  
Wright-Patterson Air Force Base, Ohio 45433

James R. Tucker  
Applied Research Associates, Inc.  
Dayton, Ohio 45433

### **Abstract**

Fires in aircraft engine nacelles must be rapidly suppressed to avoid loss of life and property. The design of new and retrofit suppression systems has become significantly more challenging due to the ban on production of Halon 1301 for environmental concerns. Since fire dynamics and the transport of suppressants within the nacelle are both largely determined by the available air flow, efforts to define systems using less effective suppressants greatly benefit from characterization of nacelle air flow fields. A combined experimental and computational study of nacelle air flow therefore has been



initiated. Calculations have been performed using both CFD-ACE (a Computational Fluid Dynamics (CFD) model with a body-fitted coordinate grid) and VULCAN (a CFD-based fire field model with a cartesian “brick” shaped grid). The flow conditions examined in this study correspond to the same Reynolds number as test data from the full-scale nacelle simulator at the 46 Test Wing. Pre-test simulations of a quarter-scale test fixture were performed using CFD-ACE and VULCAN prior to fabrication. Based on these pre-test simulations, a quarter-scale test fixture was designed and fabricated for the purpose of obtaining spatially-resolved measurements of velocity and turbulence intensity in a smooth nacelle. Post-test calculations have been performed for the conditions of the experiment and compared with experimental results obtained from the quarter-scale test fixture. In addition, several different simulations were performed to assess the sensitivity of the predictions to the grid size, to the turbulence models, and to the use of wall functions. In general, the velocity predictions show very good agreement with the data in the center of the channel but deviate near the walls. The turbulence intensity results tend to amplify the differences in velocity, although most of the trends are in agreement. In addition, there were some differences between VULCAN and CFD-ACE results in the angled wall regions due to the cartesian grid structure used by the VULCAN code. Also, the experimental data tended to show poorer resolution near the walls of the transition ducts. The increased uncertainty in the data highlights some of the challenges in getting data near the walls due to the low signal to noise ratio. Overall, this effort provided a benchmark case for both the VULCAN and CFD-ACE codes for the application of interest.



## **Acknowledgments**

This work is part of the Department of Defense's Next Generation Fire Suppression Technology Program, funded by the DoD Strategic Environmental Research and Development Program. Additional funding was provided by the USAF 46 Test Wing Aerospace Survivability and Safety Flight at Wright-Patterson Air Force Base, Ohio.

The authors would like to thank Dave Keyser (Naval Air Systems Command) for coordinating this activity and for his insight into the DoD applications. Also, the authors wish to express their appreciation to Paul DesJardin (Sandia National Laboratories) and Vernon Nicolette (Sandia National Laboratories) for their consultation on the numerical modeling and Walter Gutierrez (Sandia National Laboratories) for his previous efforts on modeling this problem. Finally, the authors would like to thank Lawrence Ash (NAVAIR) for initiating and organizing the project.

# Table of Contents

|  |           |
|--|-----------|
| <b>1. INTRODUCTION .....</b>   | <b>1</b>  |
| <b>2. EXPERIMENTAL DETAILS .....</b>                                   | <b>4</b>  |
| 2.1 QUARTER-SCALE FLOW FACILITY .....                                  | 4         |
| 2.2 INLET FLOW BOUNDARY CONDITIONS.....                                | 6         |
| 2.3 DATA ACQUISITION STRATEGY .....                                    | 6         |
| <b>3. NUMERICAL MODELING.....</b>                                      | <b>11</b> |
| 3.1 VULCAN.....  | 11        |
| 3.2 CFD-ACE .....  | 11        |
| 3.3 MODELING GEOMETRY.....   | 12        |
| <b>4. GRID STRUCTURE .....</b>   | <b>13</b> |
| 4.1 VULCAN.....  | 13        |
| 4.2 CFD-ACE .....  | 13        |
| <b>5. BOUNDARY CONDITIONS.....</b>                                     | <b>15</b> |
| 5.1 INLET BOUNDARY CONDITION.....                                      | 15        |
| 5.1.1. <i>Velocity</i> .....   | 15        |
| 5.1.2. <i>Turbulence Intensity</i> .....                               | 16        |
| 5.2 OUTLET BOUNDARY CONDITION .....                                    | 18        |
| 5.3 WALL CONDITIONS.....   | 18        |
| <b>6. RESULTS .....</b>  | <b>19</b> |
| 6.1 MEASUREMENT PLANE 1 .....  | 19        |
| 6.2 MEASUREMENT PLANE 2 .....  | 20        |
| 6.3 MEASUREMENT PLANE 3 .....  | 22        |
| 6.4 MEASUREMENT PLANE 4 .....  | 24        |
| 6.5 MEASUREMENT PLANE 5 .....  | 26        |
| 6.6 MEASUREMENT PLANE 6 .....  | 29        |
| 6.7 MEASUREMENT PLANE 7 .....  | 31        |
| 6.8 MEASUREMENT PLANE 8 .....  | 32        |
| 6.9 MEASUREMENT PLANE 9 .....  | 34        |
| 6.10 MEASUREMENT PLANE 10 .....  | 35        |
| 6.11 MEASUREMENT PLANE 11 .....  | 37        |
| <b>7. SENSITIVITY STUDY .....</b>                                      | <b>39</b> |
| 7.1 COARSE GRID RESULTS .....  | 39        |
| 7.2 ISOTROPIC TURBULENCE MODEL RESULTS.....                            | 45        |
| 7.3 K- $\omega$ AND LOW REYNOLDS NUMBER TURBULENCE MODEL RESULTS ..... | 53        |
| <b>8. SUMMARY .....</b>  | <b>56</b> |



## List of Figures

|  |    |
|--|----|
| FIGURE 2.1 - QUARTER-SCALE ENGINE NACELLE FLOW FACILITY .....  | 4  |
| FIGURE 2.2 - QUARTER-SCALE ENGINE NACELLE SIMULATOR .....  | 5  |
| FIGURE 2.3 - TRAILING EDGE OF THE CENTER BODY CONE IN THE ETD .....                                  | 5  |
| FIGURE 2.4 - SCHEMATIC OF THE FLOW FACILITY AND MEASUREMENT STATION LOCATIONS .....                  | 7  |
| FIGURE 2.5 - AN OVERVIEW OF THE OPTICAL ACCESS AND RELATIVE LDA POSITION .....                       | 8  |
| FIGURE 2.6 - LDA SYSTEM MOUNTED ON A 3D TRAVERSE .....   | 9  |
| FIGURE 4.1 - SECTION OF THE VULCAN GRID USED IN THE SIMULATION .....                                 | 13 |
| FIGURE 4.2 - SECTION OF THE CFD-ACE GRID USED IN THE SIMULATION .....                                | 14 |
| FIGURE 5.1 - INLET VELOCITY PROFILE COMPARISON .....   | 15 |
| FIGURE 5.2 - FIT OF INLET TURBULENCE INTENSITY .....   | 16 |
| FIGURE 6.1 - MEASUREMENT PLANE 1 VELOCITY COMPARISON .....   | 19 |
| FIGURE 6.2 - MEASUREMENT PLANE 1 TURBULENCE INTENSITY COMPARISON .....                               | 20 |
| FIGURE 6.3 - MEASUREMENT PLANE 2 VELOCITY COMPARISON .....   | 21 |
| FIGURE 6.4 - MEASUREMENT PLANE 2 TURBULENCE INTENSITY COMPARISON .....                               | 21 |
| FIGURE 6.5 - MEASUREMENT PLANE 3 VELOCITY COMPARISON .....   | 23 |
| FIGURE 6.6 - MEASUREMENT PLANE 3 TURBULENCE INTENSITY COMPARISON .....                               | 23 |
| FIGURE 6.7 - MEASUREMENT PLANE 3 ROOT MEAN SQUARE OF $u'_s$ COMPARISON .....                         | 24 |
| FIGURE 6.8 - MEASUREMENT PLANE 4 VELOCITY COMPARISON .....   | 25 |
| FIGURE 6.9 - MEASUREMENT PLANE 4 TURBULENCE INTENSITY COMPARISON .....                               | 25 |
| FIGURE 6.10 - MEASUREMENT PLANE 4 ROOT MEAN SQUARE OF $u'_s$ COMPARISON .....                        | 26 |
| FIGURE 6.11 - MEASUREMENT PLANE 5 VELOCITY COMPARISON .....  | 27 |
| FIGURE 6.12 - MEASUREMENT PLANE 5 TURBULENCE INTENSITY COMPARISON .....                              | 28 |
| FIGURE 6.13 - MEASUREMENT PLANE 5 ROOT MEAN SQUARE OF $u'_s$ COMPARISON .....                        | 28 |
| FIGURE 6.14 - MEASUREMENT PLANE 6 VELOCITY COMPARISON .....  | 29 |
| FIGURE 6.15 - MEASUREMENT PLANE 6 TURBULENCE INTENSITY COMPARISON .....                              | 30 |
| FIGURE 6.16 - MEASUREMENT PLANE 6 ROOT MEAN SQUARE OF $u'_s$ COMPARISON .....                        | 30 |
| FIGURE 6.17 - MEASUREMENT PLANE 7 VELOCITY COMPARISON .....  | 31 |
| FIGURE 6.18 - MEASUREMENT PLANE 7 TURBULENCE INTENSITY COMPARISON .....                              | 32 |
| FIGURE 6.19 - MEASUREMENT PLANE 8 VELOCITY COMPARISON .....  | 33 |
| FIGURE 6.20 - MEASUREMENT PLANE 8 TURBULENCE INTENSITY COMPARISON .....                              | 33 |
| FIGURE 6.21 - MEASUREMENT PLANE 9 VELOCITY COMPARISON .....  | 34 |
| FIGURE 6.22 - MEASUREMENT PLANE 9 TURBULENCE INTENSITY COMPARISON .....                              | 35 |
| FIGURE 6.23 - MEASUREMENT PLANE 10 VELOCITY COMPARISON .....   | 36 |
| FIGURE 6.24 - MEASUREMENT PLANE 10 TURBULENCE INTENSITY COMPARISON .....                             | 36 |
| FIGURE 6.25 - MEASUREMENT PLANE 11 VELOCITY COMPARISON .....   | 37 |
| FIGURE 6.26 - MEASUREMENT PLANE 11 TURBULENCE INTENSITY COMPARISON .....                             | 38 |
| FIGURE 7.1 - GRID SENSITIVITY: MEASUREMENT PLANE 1 VELOCITY COMPARISON .....                         | 40 |
| FIGURE 7.2 - GRID SENSITIVITY: MEASUREMENT PLANE 1 TURBULENCE INTENSITY COMPARISON .....             | 40 |
| FIGURE 7.3 - GRID SENSITIVITY: MEASUREMENT PLANE 3 VELOCITY COMPARISON .....                         | 41 |
| FIGURE 7.4 - GRID SENSITIVITY: MEASUREMENT PLANE 3 TURBULENCE INTENSITY COMPARISON .....             | 42 |
| FIGURE 7.5 - GRID SENSITIVITY: MEASUREMENT PLANE 7 VELOCITY COMPARISON .....                         | 43 |
| FIGURE 7.6 - GRID SENSITIVITY: MEASUREMENT PLANE 7 TURBULENCE INTENSITY COMPARISON .....             | 43 |
| FIGURE 7.7 - GRID SENSITIVITY: MEASUREMENT PLANE 11 VELOCITY COMPARISON .....                        | 44 |
| FIGURE 7.8 - GRID SENSITIVITY: MEASUREMENT PLANE 11 TURBULENCE INTENSITY COMPARISON .....            | 45 |
| FIGURE 7.9 - ISOTROPIC TURBULENT FLOW: MEASUREMENT PLANE 3 VELOCITY COMPARISON .....                 | 46 |
| FIGURE 7.10 - ISOTROPIC TURBULENT FLOW: MEASUREMENT PLANE 3 TURBULENCE INTENSITY<br>COMPARISON ..... | 46 |
| FIGURE 7.11 - ISOTROPIC TURBULENT FLOW: MEASUREMENT PLANE 5 VELOCITY COMPARISON .....                | 47 |
| FIGURE 7.12 - ISOTROPIC TURBULENT FLOW: MEASUREMENT PLANE 5 TURBULENCE INTENSITY<br>COMPARISON ..... | 48 |



|  |    |
|--|----|
| FIGURE 7.13 - ISOTROPIC TURBULENT FLOW: MEASUREMENT PLANE 7 VELOCITY COMPARISON .....  | 49 |
| FIGURE 7.14 - ISOTROPIC TURBULENT FLOW: MEASUREMENT PLANE 7 TURBULENCE INTENSITY<br>COMPARISON .....                           | 49 |
| FIGURE 7.15 - ISOTROPIC TURBULENT FLOW: MEASUREMENT PLANE 9 VELOCITY COMPARISON .....  | 50 |
| FIGURE 7.16 - ISOTROPIC TURBULENT FLOW: MEASUREMENT PLANE 9 TURBULENCE INTENSITY<br>COMPARISON .....                           | 51 |
| FIGURE 7.17 - ISOTROPIC TURBULENT FLOW: MEASUREMENT PLANE 11 VELOCITY COMPARISON .....   | 52 |
| FIGURE 7.18 - ISOTROPIC TURBULENT FLOW: MEASUREMENT PLANE 11 TURBULENCE INTENSITY<br>COMPARISONS .....                         | 52 |
| FIGURE 7.19 - $\kappa$ - $\omega$ AND LOW REYNOLDS RESULTS: MEASUREMENT PLANE 3 VELOCITY COMPARISON.....                       | 54 |
| FIGURE 7.20 - $\kappa$ - $\omega$ AND LOW REYNOLDS RESULTS: MEASUREMENT PLANE 3 TURBULENCE INTENSITY<br>COMPARISON .....       | 54 |
| FIGURE 7.21 - $\kappa$ - $\omega$ AND LOW REYNOLDS RESULTS: MEASUREMENT PLANE 3 ROOT MEAN SQUARE OF<br>$u'_s$ COMPARISON ..... | 55 |

## 1. Introduction

Fires in aircraft engine nacelles pose a considerable risk to the safety and survivability of military and commercial aircraft. Effective systems and strategies are needed to suppress or extinguish these fires prior to the infliction of significant structural damage. The design of new and retrofit suppression systems and strategies have become considerably more challenging due to the demise of Halon 1301 production dictated by the Montreal Protocol and subsequent Copenhagen amendment. Despite extensive research, alternative suppressants with a per-unit mass chemical effectiveness equivalent to Halon 1301 as well as acceptable levels of toxicity, Global Warming Potential (GWP), and Ozone Depletion Potential (ODP) have yet to be discovered. To avoid the large weight penalties of carrying additional agent, it is useful to examine additional factors that influence suppression system performance. These factors include the characterization of the fire environment (to determine actual suppressant effectiveness requirements) and the transport of suppressant (to determine how to best ensure delivery of the suppressant to the fire). Both of these factors require knowledge of the flow field in engine nacelles. Therefore, the overall objective of this study is to predict flow fields in engine nacelles. A joint experimental and computational study has been initiated, with the goal of developing validated computational models which can provide an understanding of the relevant flow features in nacelles.

The relevant region for fires in engine nacelles is the long, slender, annular, void space between the engine core and the outer aerodynamic skin. A large number of components are located within this region resulting in a complex, cluttered geometry. The nacelle design typically includes air flow, either via an external scoop or other vent air, for cooling purposes and to avoid the build-up of flammable mixtures. In general, this "engineered" air flow has sufficient momentum to dominate the buoyancy produced by burning. The dynamics of a fire within an aircraft engine nacelle are therefore typically dominated by the features of the designed air flow.

Presently, aircraft survivability and suppression system proving tests are performed under conditions intended to replicate the nacelle air flow while the aircraft is in flight. Test fixtures, such as the Aircraft Engine Nacelle Fire Test Simulator (AENFTS) facility at the 46 Test Wing Aerospace Survivability and Safety Flight at Wright-Patterson Air Force Base (WPAFB) in Dayton Ohio, have been constructed to represent the long, slender, geometries typical of aircraft nacelles. Extensive sets of experiments (with varying degrees of complexity in the internal geometry) have been conducted



to evaluate the performance of fire suppression systems and strategies. These tests and experiments have provided significant insight into the essential and salient features of successful suppression systems, and serve as the basis for present system acceptance. However, the results from these tests, particularly when fire extinguishment (as opposed to cold flow tests) is the focus, are often difficult to understand due to the lack of a well-characterized flow field.

Due primarily to geometric complexities, efforts to characterize the flow field in engine nacelles using computational fluid dynamics (CFD) have been limited to simplified cases. Previous calculations performed to date include analysis performed by Hamins et al. [1] of agent transport for the extensive set of tests performed in the AENFTS for the Halon Alternatives Research Program for Aircraft Engine Nacelles and Dry Bays [2, 3]. These calculations were performed using the commercially-available CFX model. Marginal agreement between calculation results and experimental data was obtained. In some cases, opposite trends were observed in the calculations and experimental results. Additional calculations of a smooth F18 nacelle geometry with agent release via solid propellant gas generator were performed by Lopez et al. [4]. Results from this analysis were consistent with trends observed in data from simulator tests at the Naval Air Warfare Center at China Lake. Sufficient data were not available to rigorously validate the model predictions.

Given the limited available data, and the difficulties encountered in validating model calculations for simplified cases with the same inherent features as actual nacelles, the present effort employs a combined experimental and computational approach. This study will begin with experiments and model calculations for the flow in a smooth slender annular geometry. Although fully developed flows in annuli are well understood, the development of those flows, with different inlet conditions, has yet to be addressed.

In the present work, reduced (1/4) scale experiments (to allow access of appropriate diagnostics), guided by pre-test calculations, were performed at the 46 Test Wing in a smooth slender annular geometry. Flow conditions were Reynolds number scaled to match the extensive set of experiments performed in the AENFTS as part of the Halon Alternatives Research Program for Aircraft Engine Nacelles and Dry Bays [2, 3]. Calculations were performed and compared with experimental data at multiple cross sections within the flow field. Once confidence in the model and measurements, and a confirmed understanding of the flow field, has been obtained for this general class of problems, complex geometries more representative of actual aircraft nacelles will be addressed. During the first stage of this endeavor, pre-test



calculations were performed to assist in the design and execution of the experiments. These experiments were required to gain the necessary knowledge and validation data for this class of flows. Based on the pre-test calculations, a test fixture was designed and experiments were conducted to characterize the flow in the smooth nacelle. Post-test simulations were conducted using both CFD-ACE and VULCAN for the conditions of the experiments. This report presents the results from the post-test simulations using the geometry and boundary conditions from the experiments and compares the CFD code results with the experimental measurements.

The primary flow field calculations presented here were performed using the CFD-ACE model. The model features body-fitted coordinates which accurately represent smooth circular geometries. Although capable of simulating reacting flows, the CFD-ACE code does not contain the models for participating media radiation heat transfer, turbulent combustion, and soot needed to simulate fires. These fire physics models are included in the VULCAN fire field model, but the VULCAN model approximates the geometry using a rectangular "brick" grid to facilitate rapid solution of participating media radiation. Although many nacelle fire cases can be addressed without modeling the fire physics [4], it is ultimately desirable to be able to represent the heat transfer from the fire and fire suppression effects, such as the influence of turbulent flame strain combined with fuel/air mixture fraction. Both models have therefore been applied in the pre-test and post-test calculations. The flow solution yielded by the approximate mesh used in the VULCAN code is compared with the results provided by the CFD-ACE modeling to quantify the effect of the more rudimentary VULCAN mesh. In an attempt to validate the CFD codes, results from both codes are compared to experimental results. Additional simulations were also performed to assess the sensitivity of the predictions to the grid size, to the turbulence models, and to the use of wall functions.

## 2. Experimental Details

### 2.1 Quarter-Scale Flow Facility

The quarter-scale flow facility (Figure 2.1) is located in Range A of the Aircraft Survivability Research Facility at WPAFB. The facility consists of an external blower, a flow conditioning section, a quarter-scale nacelle test section, and optical measurement diagnostics. Ambient air is supplied to the facility using an external blower. The air is drawn into the blower inlet and directed to the quarter-scale nacelle simulator through a combination of 152.4 mm (6 in ID) PVC plastic and acrylic tubing. To prevent blower vibrations from being transferred to the simulator, a flexible rubber expansion joint was placed between the blower exit and the PVC air supply tube. At the exit of the supply tube, the flow enters a conditioning section consisting of stainless-steel tubes and fine mesh stainless steel screens to minimize flow disturbances introduced by the blower. After exiting the conditioning section, the air stream travels an additional 45 diameters to the nacelle inlet transition duct (ITD).

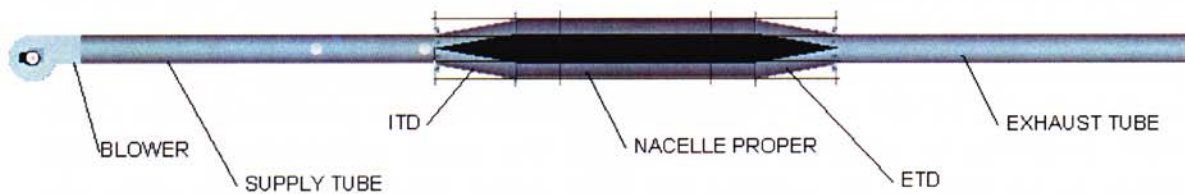
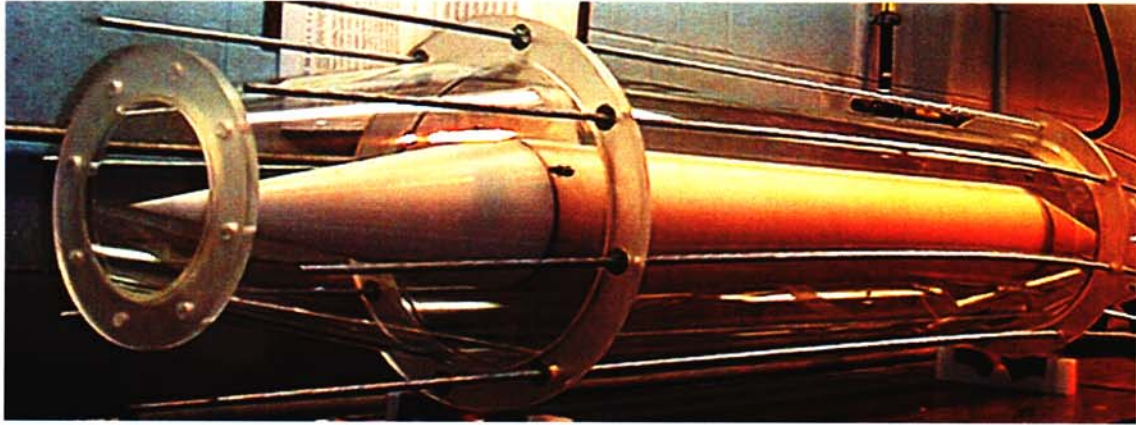


Figure 2.1 - Quarter-scale engine nacelle flow facility

At the entrance to the ITD, the flow undergoes a change from pipe flow to diverging annular flow. This change in flow field geometry is accomplished using a machined Teflon cone, with a sharp leading edge, centered within the ITD. The cone is approximately 432 mm (17 in) long and 149.4 mm (5.88 in) wide and is attached to the 149 mm Teflon core that resides within the nacelle. The cone half angle was machined at 10 degrees. The combination of cone angle and ITD wall offset redirects the flow away from the simulator centerline (Figure 2.2) and increases the cross-sectional area by a factor of approximately three. This geometric change occurs abruptly at the interface between the air supply duct and ITD, and is therefore considered to be a sharp or discontinuous surface boundary.





**Figure 2.2 - Quarter-scale engine nacelle simulator**

After passing through the ITD, the flow is abruptly redirected inward by 10 degrees into a straight annular section. The redirection of flow is discontinuous on both the inner surface (simulating the scaled engine core) and outer duct surface (simulating the scaled engine nacelle). The straight annular section, referred to as the nacelle proper, has a constant spacing ( $H$ ) of 74.7 mm (2.94 in) and extends downstream 1.22 m (48 in), or approximately 16  $H$ .

After exiting the nacelle section, the flow enters the Exit Transition Duct (ETD) and is redirected inward 10 degrees toward the simulator centerline. At the entrance of the ETD, the inner core undergoes a sudden transition back to a conical surface with a sharp trailing edge (Figure 2.3), thereby producing a converging annular section.

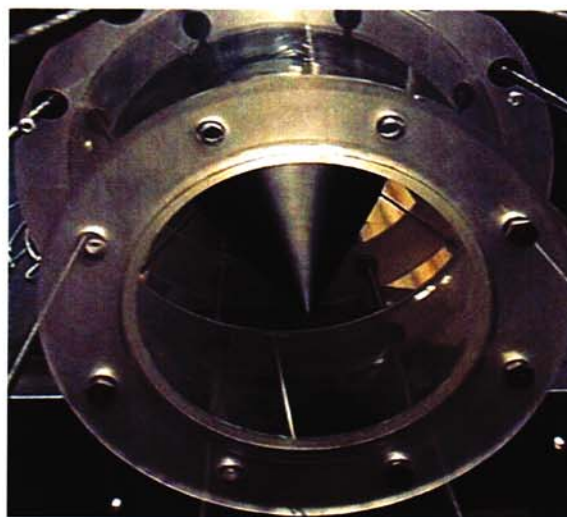


**Figure 2.3 -Trailing edge of the center body cone in the ETD**



At the exit of the ETD, a transition occurs through a surface discontinuity from a converging annulus channel to a straight exhaust tube. This 152.4 mm (6 in) diameter exhaust tube extends downstream approximately 40 diameters before undergoing a sudden enlargement where the exiting air expands into a PVC tube with an internal diameter of 30.5 cm (12 in) and is directed outside of the test chamber.

## **2.2 Inlet Flow Boundary Conditions**

Flow conditions upstream of the quarter-scale engine nacelle were determined by matching the Reynolds number (based on the diameter in the annular region) between the full-scale and quarter-scale nacelle simulators, for a specified mass flow rate. Air at ambient temperature and pressure ( $T_{amb}$  and  $P_{amb}$ ) was used to supply the flow facility in all tests. Supply air density was computed using the local temperature and pressure of the surrounding air. Typical values of  $P_{amb} = 98.7$  kPa (14.37 psia) and  $T_{amb} = 293$  K (73 °F) resulted in a computed density of  $1.2$  kg/m<sup>3</sup> (0.0748 lbm/ft<sup>3</sup>). From this density, a mass flow rate of  $0.344$  kg/s (0.757 lbm/s) was determined for the quarter-scale nacelle. Assuming uniform flow, the average velocity within the 152.4 mm (6 in) air supply tube was  $15.7$  m/s (51.5 ft/s). Under these conditions the inlet flow Reynolds number based on tube diameter,  $Re_D$ , was estimated to be 172,000.

## **2.3 Data Acquisition Strategy**

Velocity traverses across the inlet air supply tube, as well as several locations throughout the expansion and contraction annular regions, were taken using Laser Doppler Anemometry (LDA) configured in backscatter mode. Velocity and turbulent intensity profiles were obtained at 11 measurement stations as determined from pre-test calculations. Table 2.1 provides a complete listing of the LDA measurement stations along with their relative streamwise location. Measurement locations, designated by MS-1 through MS-11, are also presented schematically in Figure 2.4. It is important to note that MS-1 and MS-2 are located upstream of the inlet cone and therefore these stations are listed as negative quantities.

| LV Measurement Station Locations |  | locations w.r.t. core tip |         |
|----------------------------------|--|---------------------------|---------|
| Station                          | Description  | mm                        | inches  |
| Reference                        | Cone LE downstream from flow conditioner exit        | -6832.6                   | -269    |
| MS-1                             | Upstream from Cone LE                                | -619.125                  | -24.375 |
| MS-2                             | -47mm (-1.875") Upstream from Cone LE                | -47.625                   | -1.875  |
| Reference                        | Start of ITD   | -1.016                    | -0.04   |
| Reference                        | Start Cone/Engine Core LE                            | 0                         | 0       |
| MS-3                             | Downstream from Cone LE and within the ITD           | 60.325                    | 2.375   |
| MS-4                             | Downstream from Cone LE and within the ITD           | 196.85                    | 7.75    |
| MS-5                             | Downstream from Cone LE and within the ITD           | 314.325                   | 12.375  |
| Reference                        | Nacelle Proper/ITD surface discontinuity (End ITD)   | 415.036                   | 16.34   |
| Reference                        | Cone TE  | 428.752                   | 16.88   |
| MS-6                             | Downstream of ITD/Nacelle surface discontinuity      | 457.962                   | 18.03   |
| MS-7                             | Downstream of ITD/Nacelle surface discontinuity      | 1028.7                    | 40.5    |
| MS-8                             | Downstream of ITD/Nacelle surface discontinuity      | 1596.136                  | 62.84   |
| Reference                        | Nacelle Proper/ETD surface discontinuity (Start ETD) | 1634.236                  | 64.34   |
| Reference                        | Start Cone/Engine Core LE                            | 1634.236                  | 64.34   |
| MS-9                             | Downstream from Nacelle/ETD surface discontinuity    | 1831.086                  | 72.09   |
| Reference                        | End of ETD   | 2050.288                  | 80.72   |
| Reference                        | Cone/Engine core Trailing edge (TE)                  | 2066.036                  | 81.34   |
| MS-10                            | Downstream from Cone TE                              | 2116.836                  | 83.34   |
| MS-11                            | Downstream from Cone TE                              | 2675.636                  | 105.34  |
| Reference                        | Sudden expansion from 6" to 12" PVC exhaust duct     | 8771.636                  | 345.34  |

Note:

LE - Leading Edge

TE - Trailing Edge

ITD - Inlet Transition Duct

ETD - Exit Transition Duct

**Table 2.1 - Locations of Measurement Stations**

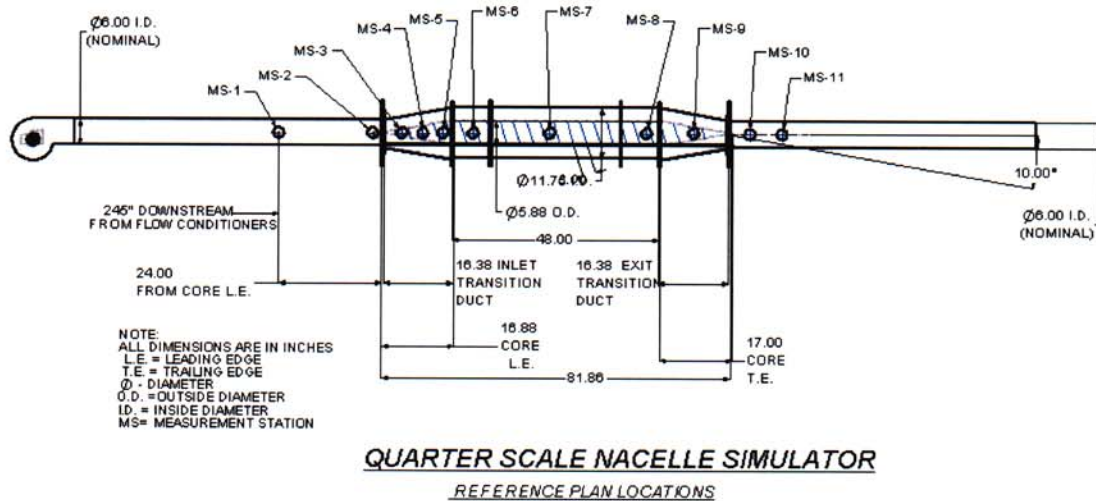


**Figure 2.4 - Schematic of the flow facility and measurement station locations**



Velocity data acquired at stations MS-1 and MS-2, in the air supply tube, document the conditions of the approach flow and MS-1 serves as the inflow boundary condition for the CFD calculations. Measurement station 1 was located 40.8D (6.2 m or 245 in) downstream from the flow conditioning section, and MS-2 was 44.8D downstream. The relative locations of stations 1 and 2 were therefore positioned upstream of the inlet transition duct (ITD) by -629 mm (-24.76 in) and -47 mm (-1.87 in), respectively.

To enable LDA measurements in the presence of the curved surfaces that comprise the simulator, flat removable windows were installed into machined openings at each measurement station. Windows were installed such that the intrusion into the flow field was minimal, resulting in a 1.6 mm reduction in the effective diameter at the measurement plane. The following image provides an overview of the optical access available within the simulator and the relative location of the LDA system (Figure 2.5).

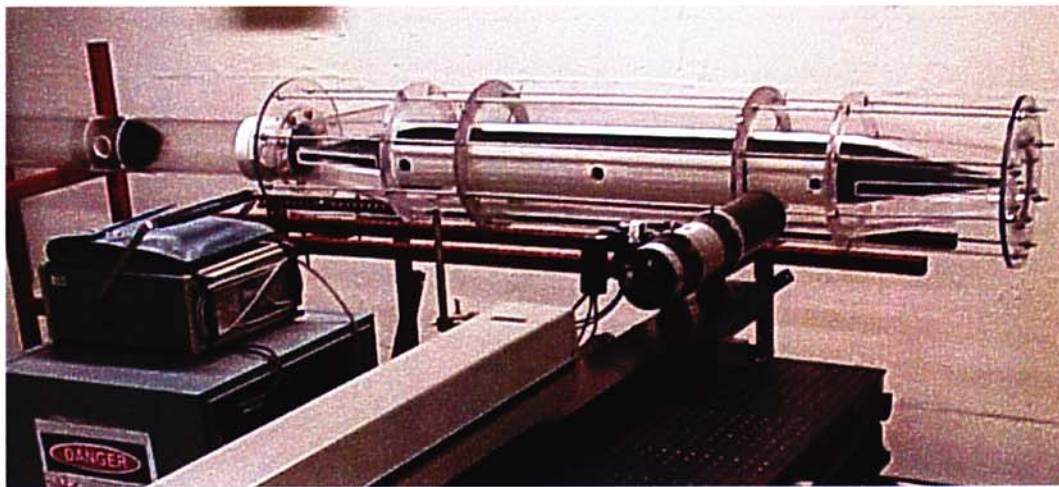


**Figure 2.5 - An overview of the optical access and relative LDA position**

During each experiment, the blower speed was set to the desired mass flow rate and the local air speed within the supply tube was continually monitored using a pitot-static pressure probe connected to a differential magnetic pressure gage. For reference purposes, the probe was positioned within the air supply tube approximately 40 mm away from the tube wall and approximately 20D downstream of the flow conditioning section.

Velocity profile data were acquired using a Dantec 55X laser Doppler anemometry system (LDA) with illumination from an Argon-Ion laser operating at 488nm (blue component) and 514.5 nm (green component). The LDA system was configured in the backscatter mode, with a focal length of 310 mm (12.25 in), and was mounted on an optical bench with three degrees



of freedom. Spatial positioning of the LDA measuring volume was obtained by manual adjustment of the bench using an xyz traverse (Figure 2.6) with a range of approximately 305 mm (12 in) in each of the three directions. The spatial resolution in the x-y plane (a plane parallel to the nacelle centerline) was nominally  $\pm 127$  microns (0.005 in), and the vertical or z component was  $\pm 2.5$  mm (0.1 in).



Figure 2.6 - LDA system mounted on a 3D traverse

LDA measurements were performed in only one spatial direction. Given the optical configuration of the present LDA system, measurement volume dimensions of approximately 86 microns in diameter and 0.735 mm in length were estimated. Scattered signals from the photo detectors were frequency shifted by 40 MHz and passed to a counter type signal processor. Tests were conducted with the current LDA setup to determine the number of samples necessary to provide repeatable data. Higher data rates resulted from the selection of the green laser beam component at 514.5 nm. Sample sizes of 300, 400, and 500 were evaluated and found to differ by less than 6 cm/s. The present LDA acquisition system was therefore set to acquire 300 data points at each spatial location. To provide additional confidence in the LDA data, several velocity traverses were acquired at most measurement stations. Typically, each velocity traverse consisted of 45 spatial locations measured across the diametrical plane of the tube. In addition, at each measurement station, the LDA optics was reoriented such that the each traverse was always performed normal to the streamwise flow direction.

LDA measurements are based on the ability to adequately seed the flow field of interest with micron-sized particles. Seed material in the present study was generated by the vaporization of a solution mixture (75% propylene glycol and 25% water) using a commercial smoke generator. The fog was introduced at the blower inlet producing a well-mixed, densely seeded, flow at the blower exit with nominal particle sizes between 1 and 6 microns. Stokes

number estimates ranged from 0.006 in the central region of the tube to 0.13 at the walls. Statistical uncertainty in the mean velocity measurements varied between  $\pm 0.27$  m/s in the nacelle region to  $\pm 0.22$  m/s in the core region. It was unclear how to quantify the statistical uncertainty of the turbulence intensity data directly from the LDA measurements; however, hot wire measurements of the turbulence intensity were compared to the LDA values at the same location and found to be within 10% of one another.

The measurement uncertainty with the LDA experiments is difficult to quantify and is not provided. It should be noted that LDA systems do not need to be calibrated; however, hot-wire traverses were performed at the same locations (i.e., MS-1 and MS-2) and found to be in good agreement with the LDA data. In addition, repeatability tests were performed and found to be in good agreement. At MS-2, measurements were taken on two different days and the data showed an 8% difference in mean velocity and 24% difference in turbulence intensity.



### 3. Numerical Modeling

Post-test calculations of the flow in a quarter-scale nacelle have been obtained using both the VULCAN and CFD-ACE models. The CFD-ACE code is best suited for numerical simulation of flows in complex geometries. VULCAN includes submodels required to simulate flow and fire dynamics phenomena and therefore makes some approximations to represent complex geometries. Notable differences between VULCAN and CFD-ACE include the Cartesian grid as opposed to the body-fitted coordinate system in CFD-ACE and the ability to model fires with VULCAN, which is not possible with CFD-ACE. This section provides additional background information on each code.

#### 3.1 VULCAN

VULCAN has been developed over the past 8 years at Sandia National Laboratories (SNL). VULCAN is derived from the KAMELEON fire model from the SINTEF Foundation and the Norwegian University of Science and Technology (NUST) [5,6] and uses an extension of the SIMPLEC method of Patankar and Spalding [7] to solve the conservation equations on a structured, staggered, three-dimensional Cartesian grid. The “brick” mesh is employed in part to facilitate rapid solutions of participating media radiative heat transfer. The ability to resolve the geometry of the system is only limited by the ability to construct the appropriate grid with the Cartesian grid generator available in VULCAN. A second-order accurate upwind scheme is used for the convective terms. Turbulence is modeled using a standard two equation  $k$ - $\epsilon$  model with wall functions. Combustion is based on Magnussen’s Eddy Dissipation Concept [6] with infinitely fast combustion assumptions. Models of soot generation and oxidation are also included.

#### 3.2 CFD-ACE

CFD-ACE is a pressure-based commercial code [8,9] that solves the Farve-averaged Navier-Stokes equations. The code uses a cell-centered control volume approach to discretizing the governing equations. It employs an iterative solution scheme in which the assembled equations for each dependent variable are solved sequentially and repeatedly to reduce errors to acceptably low values.

Various modeling options are available. In the present calculations, the governing equations were solved until a steady-state solution was reached. Heat transfer was not modeled. The code was applied using the incompressible option with a single fluid (air) and the  $k$ - $\epsilon$  turbulence model of Launder and Spalding [10] with wall functions. In addition, the  $k$ - $\omega$  turbulence model of Wilcox [11] and the Low Reynolds number  $k$ - $\epsilon$  turbulence

model of Chien and Smith [12] were used in sensitivity calculations. First-order upwind spatial differencing was used for the turbulence quantities and 90% second-order upwind spatial differencing (with 10% first order blend) was used for the velocity and density. The structured grid utilized a body-fitted coordinate system with multiple domains.

### **3.3 Modeling Geometry**

The geometry used in the fluid flow simulations was a quarter-scale version of a representative full-scale nacelle geometry, slightly revised for modeling purposes. To ensure consistency with the existing data [13], the full-scale nacelle geometry has the same basic dimensions as the nacelle simulator section used in the AENFTS for the Halon Alternatives program. Enhancements include the reduction of geometric complexity posed by viewports on the outer walls. The surface-of-revolution geometry considered in these analyses do not contain any internal clutter. Nomenclature for primary parts are the inlet pipe, outlet pipe, nacelle and core. Figure 2.4 provides the dimensions for the pipes, nacelle, and the core. The presence of wires or struts used to support the core were neglected in the simulations. All corners and tips have been considered sharp (i.e. - radius of zero). The windows in the nacelle wall were not modeled. It should be noted that the nacelle geometry was modeled starting at measurement station #1, where experimental data were acquired to use as exact input. None of the inlet flow conditioning screens, honeycombs (tubes), etc. were modeled. The modeled geometry ended 10 pipe diameters downstream of the core region, which is 6 pipe diameters downstream of the final measurement station (MS-11).



## 4. Grid Structure

### 4.1 VULCAN

VULCAN uses a cartesian grid system that induces some inaccuracies in the representation of the geometry for the expansion and contraction regions of this configuration. The transition regions appear as “stairs” rather than straight, angled lines. A portion of the grid is shown in Figure 4.1. The grid was refined in selected areas, such as the transition regions, allowing the important flow characteristics to be determined. In areas where the geometry was straight, such as the inlet, exit, and annular regions, the computational cells were stretched.

The length of the geometry created a grid with many computational cells. The grid was generated using the VULCAN Graphical User Interface. The final Cartesian grid consisted of 196 (X-direction) by 45 (Y-direction) by 45 (Z-direction) grid points for a total of 396,900 cells in the simulation. The cells in the cross-section were  $0.007 \times 0.007 \text{ m}^2$ , while the minimum cell length in the axial direction was 0.0085 m and varied along the pipe (refined in transition regions and stretched in the exit pipe and other straight sections). An attempt was made to use the same number of grid points and spacing as the CFD-ACE grid in order to have a one to one comparison. However, due to resource constraints, only one grid solution was obtained with VULCAN. The simulation time was approximately 5 days on an UltraSPARC 250 MHz processor. The solution was iteratively converged such that all residuals were reduced 5 orders of magnitude.

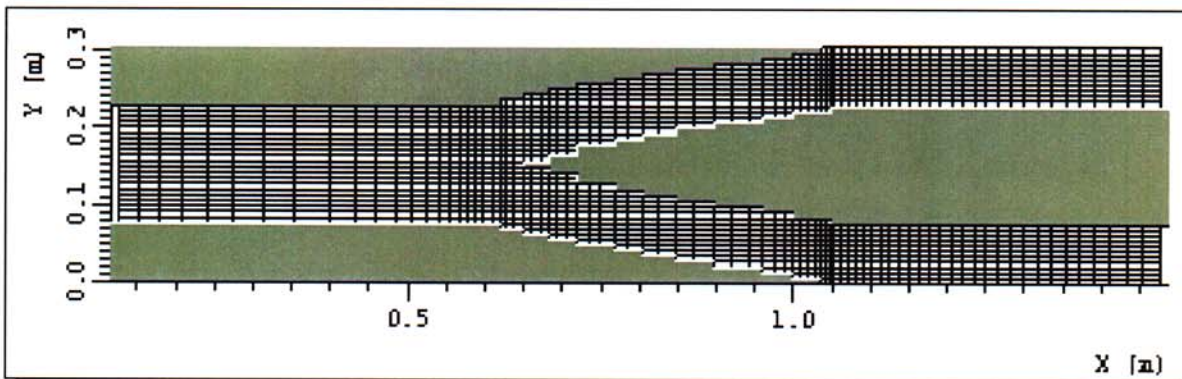
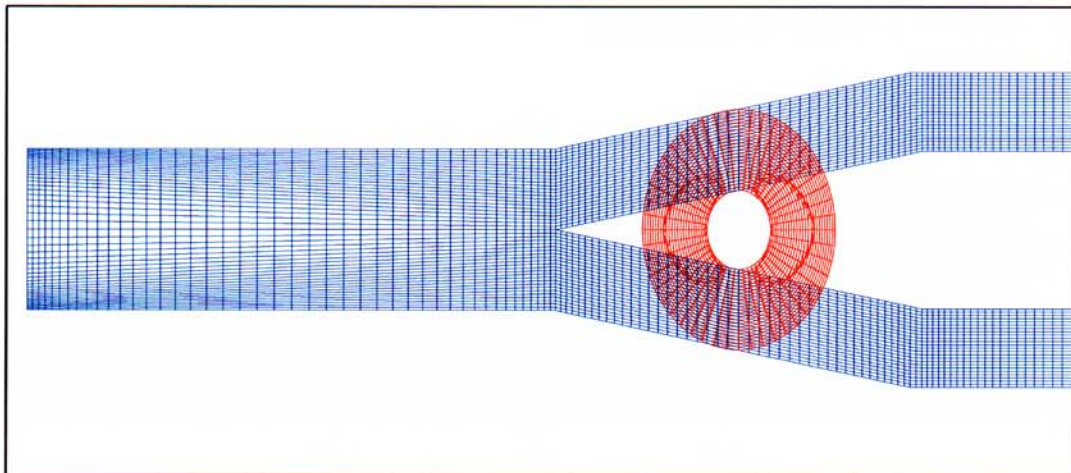


Figure 4.1 - Section of the VULCAN Grid Used in the Simulation

### 4.2 CFD-ACE

The computational grid used in CFD-ACE calculation was generated with the commercial code Gridgen [14]. A three-dimensional (3-D) grid was used in the

simulation instead of an axisymmetric grid, in order to capture any potential swirling flow which may have resulted due to flow conditioners, and also to allow for future 3-D geometric features. The structured, three-dimensional (3-D), multi-block grid consisted of 301 axial (primary flow direction) points, 25 radial points, and 48 circumferential points, for a total of 361,200 grid points. Example slices from the grid are shown in Figure 4.2. Axial grid spacing in the annular (nacelle/core) region varied from 0.006 m (0.25 in) near the corners of expansion/contraction to 0.018 m (0.69 in) in the middle section of constant diameter flow. Radial spacing was approximately 0.002 m (0.08 in) throughout the annulus. Circumferential spacing was constant at 7.5 degree increments which relates to linear (arc) dimensions of 0.020 m (0.77 in) at the maximum nacelle diameter to 0.010 m (0.39 in) at the maximum core diameter. In addition to the 'fine' three-dimensional (3-D) grid solution, a coarser mesh solution (ACE-Coarse) was obtained. The coarse mesh was generated by extracting every other grid point in all three directions from the fine mesh. The coarse mesh contained 151 axial points, 13 radial points, and 24 circumferential points, for a total of 47,112 grid points. In both mesh simulations, iterative convergence was obtained such that all residuals of interest (velocity, pressure, turbulence) were reduced more than 5 orders of magnitude. The fine mesh solution required 400 Mbytes of memory, 2200 iterations and 15 days computing time on a Sun Microsystems UltraSPARC 250 MHz processor, while the coarse mesh solution required less than 1 day of computing time.



**Figure 4.2 - Section of the CFD-ACE Grid Used in the Simulation**



## 5. Boundary Conditions

The boundary conditions used in the 3-D turbulent CFD simulations were applied to best represent the experimental conditions. In some cases, a slight deviation from the experimental conditions was necessary. The boundary conditions will be fully discussed in this chapter. Comparison with the exact experimental conditions at the inlet will also be made.

### 5.1 Inlet Boundary Condition

#### 5.1.1. Velocity

The experimental data measured at the inlet (MS-1) showed a slight asymmetry in the velocity profile. It was not possible to specify this asymmetric velocity profile as an inlet boundary condition in the calculations since only a radial profile was allowed by CFD-ACE. Instead, a symmetrical profile (log-law relationship:  $u/u_{\max} = (y/R)^{0.12}$ ) was used and the agreement with the measured inlet profile is shown in Figure 5.1. In both cases, the maximum velocity is 20.07 m/s.

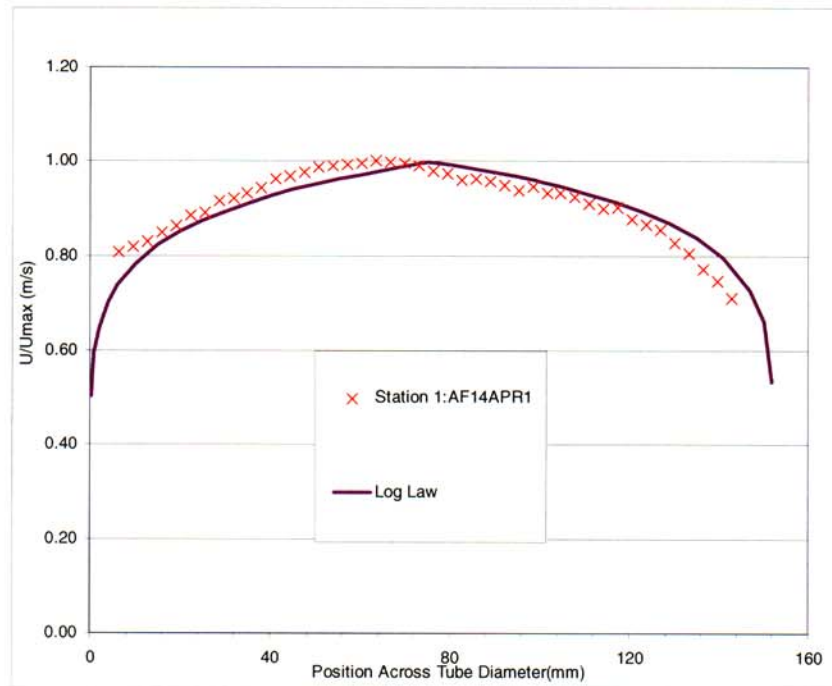


Figure 5.1 - Inlet Velocity Profile Comparison

### 5.1.2. Turbulence Intensity

Similar to the inlet velocity, the measured inlet turbulence intensity was also asymmetric. The boundary condition for the calculations used a symmetric inlet turbulent intensity based on a parabolic curve fit of experimental data. This was accomplished by splitting the experimental data set at the midpoint, mirroring both sides across the centerline, and fitting a parabolic curve to the resulting data set (see Figure 5.2). The resulting equation for the inlet turbulence intensity is shown on the plot.

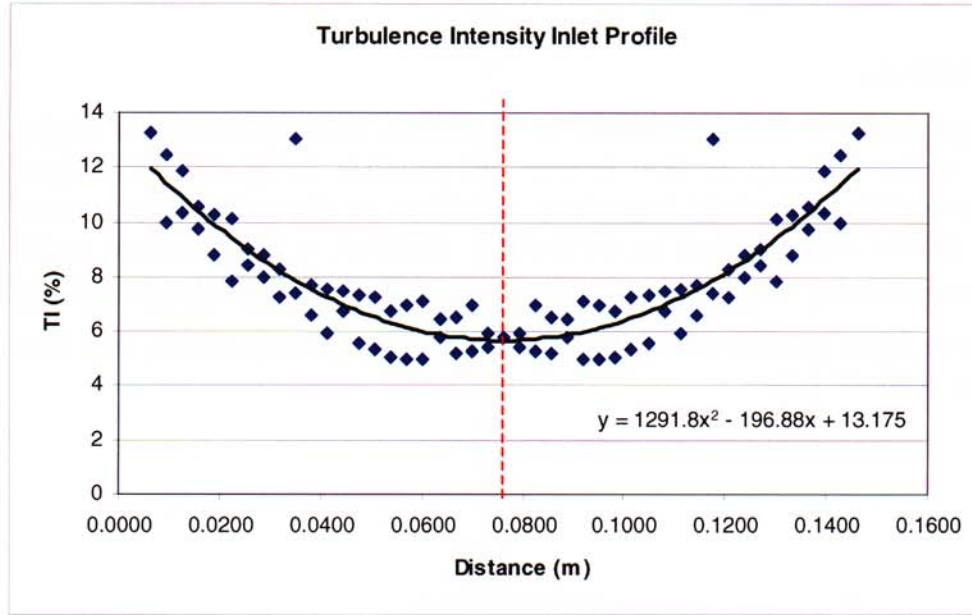


Figure 5.2 - Fit of Inlet Turbulence Intensity

Turbulence intensity is not a direct variable used in the codes and approximations must be introduced in order to relate the experimental definition of turbulence intensity to that employed in the codes. In the experiment, turbulence intensity,  $I$ , is determined from the measurements using the following equation:

$$I = \frac{\sqrt{\overline{u_s'^2}}}{\overline{u_s}}$$

The bar symbol represents the mean of the squared value,  $u_s'$  is the fluctuating stream-wise velocity, and  $\overline{u_s}$  is the mean flow stream-wise velocity. In the  $k$ - $\epsilon$  turbulence model, the definition of the turbulent kinetic energy is:



$$k = \frac{\overline{u'^2} + \overline{v'^2} + \overline{w'^2}}{2} = \frac{\overline{u_s'^2} + \overline{v_c'^2} + \overline{w'^2}}{2}$$

Since  $v_c'$  and  $w'$  are not measured in the experiment, approximations are required to relate  $u_s'$  to  $k$ . Two approaches were explored. The first approach assumed that all cross-stream velocity fluctuations were zero, i.e.  $v_c' = w' = 0$ . Using the experimental definition of turbulence intensity, the turbulent kinetic energy becomes:

$$k = \frac{\overline{u_s'^2}}{2} = \frac{(I\overline{u_s})^2}{2}$$

Both the VULCAN and the CFD-ACE calculations used the first approach to define the turbulent kinetic energy at the inlet plane and to solve for the turbulence intensity from the turbulent kinetic energy calculated at each measurement plane. Experimental observations conjecture that the cross-stream velocity fluctuations were very small based on random cross-stream velocity measurements [15].

The second approach assumed turbulent isotropic flow, i.e.,  $u_c' = w' = u_s'$ . Again using the experimental definition of turbulence intensity, the turbulent kinetic energy becomes:

$$k = \frac{3\overline{u_s'^2}}{2} = \frac{3(I\overline{u_s})^2}{2}$$

Another CFD-ACE calculation (ACE-Turbulence) using the second approach was performed in order to understand the effect of the turbulence model approximations on the flow field velocity. Results for both turbulence cases will be discussed in Section 7.

It should be noted that an underlying assumption of the k- $\epsilon$  model is that the fluctuating velocity components contribute equally to the turbulent kinetic energy [16]. This is consistent with the turbulent isotropic flow assumption. However, assuming that the turbulent kinetic energy is equipartitioned is considered a shortcoming of the model since this is not consistent with either experiment or more advanced theories. In Section 7.2, the turbulent model comparisons show that the assumption of zero cross-stream fluctuating velocities is in better agreement with the data than the isotropic flow relation.

## **5.2    *Outlet Boundary Condition***

At the outlet of the nacelle geometry, a constant pressure condition was specified using ambient conditions of 98,700 Pa and 293 K. The outlet was located 10 pipe diameters downstream of the nacelle/core region, which is 6 pipe diameters downstream of the final measurement plane (MS-11).

## **5.3    *Wall Conditions***

Along each surface of the nacelle geometry, a no-slip wall was specified at a constant temperature of 293 K. Surface roughness was not included in either simulation. In addition, wall functions were used to represent the flow next to the wall when the  $k$ - $\epsilon$  turbulence model was employed; otherwise, the solution was directly integrated to the wall when either the  $k$ - $\omega$  turbulence model or the Low Reynolds number  $k$ - $\epsilon$  turbulence model were employed.



## 6. Results

VULCAN and CFD-ACE calculations of air flow in a smooth nacelle geometry were performed. The stream-wise velocity component and turbulence intensity values were measured in the experiment conducted at 46 Test Wing at Wright Patterson Air Force Base [13]. A comparison of the numerical predictions and the experimental data at eleven measurement stations were performed. The exact measurement locations and geometric reference locations are shown in Table 2.1. The results shown below are for a vertical slice through the geometric centerline at each location. The VULCAN results are based on values at cell centers while the CFD-ACE results are based on values at the grid points.

### 6.1 Measurement Plane 1

Figures 6.1 and 6.2 show the velocity and turbulence intensity for VULCAN and CFD-ACE at the inlet plane of the calculation. In Figure 6.1, the experimental data and a log-law fit of the data are compared to the specified numerical boundary conditions. As expected, both VULCAN and CFD-ACE agree exactly with the log-law fit of the data. The experimental velocity profile is slightly asymmetric and this feature was not included in the CFD simulations. Figure 6.2 also shows exact agreement between the CFD codes and the parabolic fit of the data, with the experimental data again showing a slightly asymmetric turbulence intensity profile.

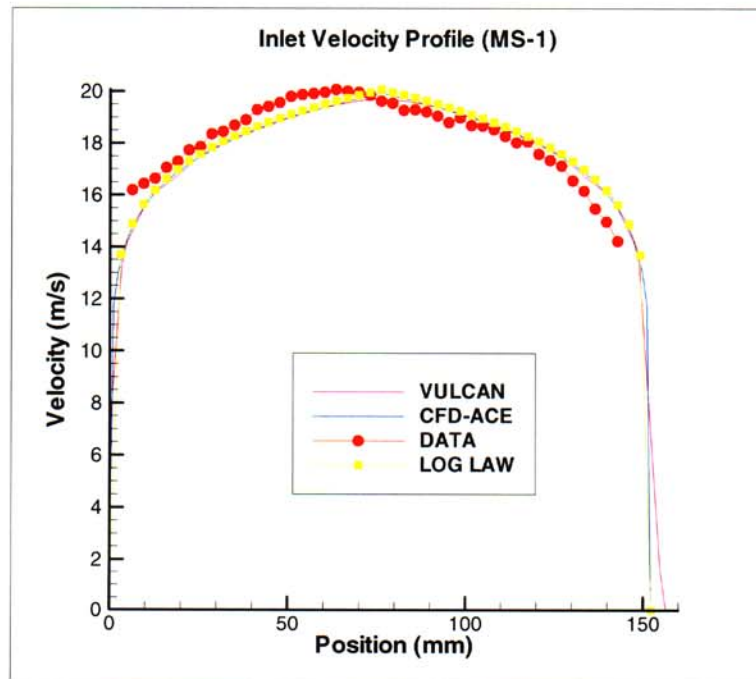


Figure 6.1 - Measurement Plane 1 Velocity Comparison

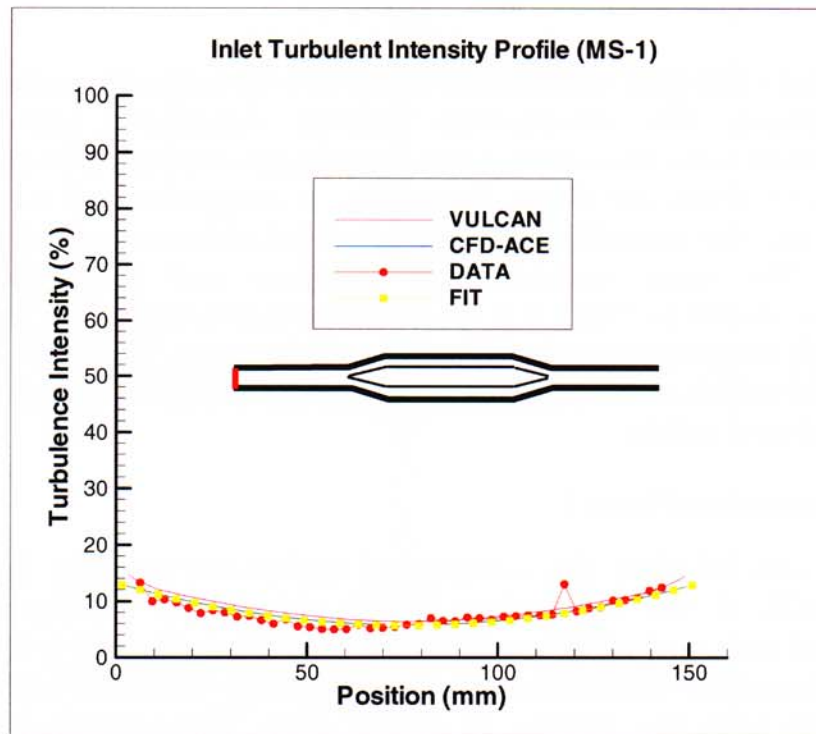
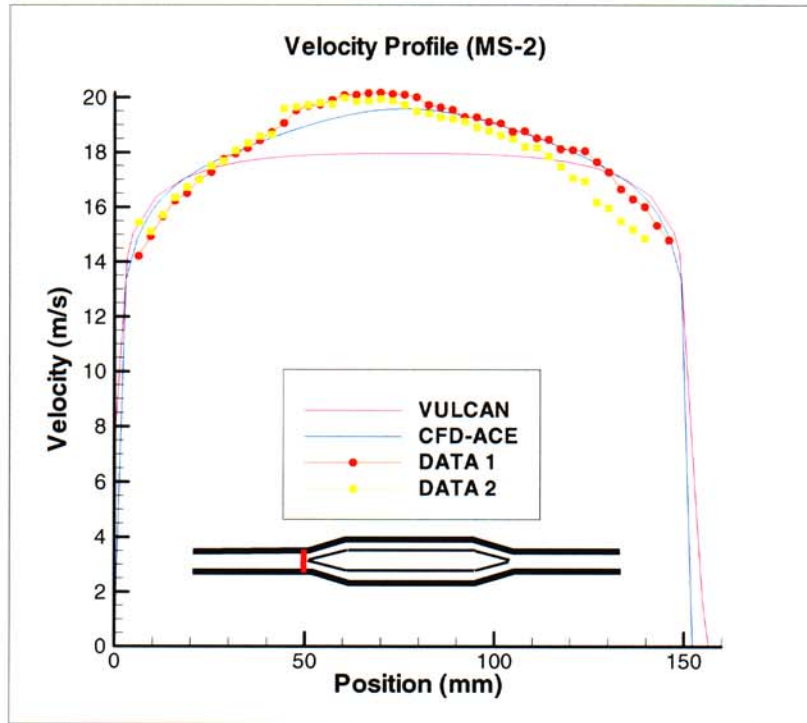


Figure 6.2 - Measurement Plane 1 Turbulence Intensity Comparison

## 6.2 Measurement Plane 2

Figures 6.3 and 6.4 show the velocity and turbulence intensity predicted by VULCAN and CFD-ACE at a location in the inlet pipe just ahead of the core tip. In addition, there are two sets of experimental data (DATA 1 and DATA 2) shown in these figures. These data were taken on different days and therefore they give an indication of the repeatability of the tests. Uncertainty in the measured mean velocity was estimated at  $\pm 0.27\text{m/s}$ . In both the velocity and turbulence intensity comparisons, the CFD-ACE prediction shows very good agreement with the experimental data, while the VULCAN prediction shows a flattening of both profiles in the center of the pipe.





**Figure 6.3 - Measurement Plane 2 Velocity Comparison**

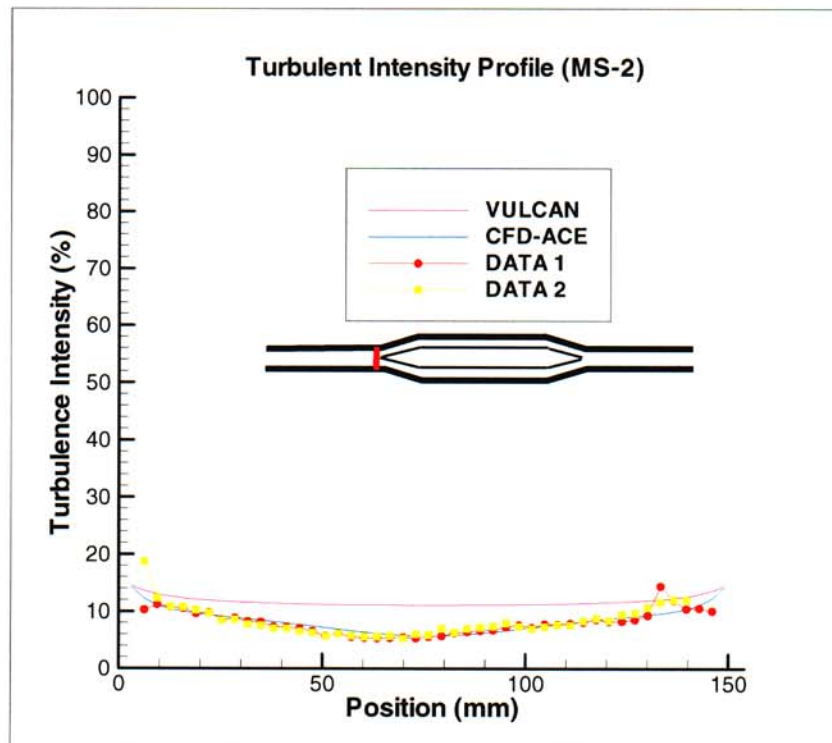


**Figure 6.4 - Measurement Plane 2 Turbulence Intensity Comparison**

### 6.3 Measurement Plane 3

Figures 6.5 and 6.6 show the velocity and turbulence intensity predicted by VULCAN and CFD-ACE at the first measurement plane in the transition region of the core. In the core region, the position ranges from 0.0 at the nacelle wall to 76.2 mm at the core wall. As shown in Figure 6.5, both sets of velocity predictions agree well with experimental data. Although the VULCAN prediction and the data appear to be in closer agreement near the walls, VULCAN does not have adequate resolution in the wall regions due to the cartesian grid structure and therefore this agreement is fortuitous. The data also show a reduction in velocity and then a slight increase near the core wall. This feature may possibly be due to a slight misalignment between the core and the flow direction. A slight misalignment would cause the flow on the leeward side of the core to separate. In addition, it should be noted that the VULCAN velocity profile in this figure does not go to zero because the end point values displayed are not exactly at the wall. In Figure 6.6, both code predictions compare well overall with the turbulence intensity data. The CFD-ACE predictions deviate from the data and the VULCAN result by ~10% near both the nacelle wall and the core wall. This difference is to be expected, given that the turbulence intensity is normalized by the mean flow velocity and the CFD-ACE prediction shows higher velocities next to the walls (in Figure 6.5). Figure 6.7 shows a plot of the root mean square (rms) of the fluctuating streamwise velocity ( $u'_s$ ) or the numerator of turbulence intensity. For this quantity, the CFD-ACE prediction shows much better agreement with the experimental data. Statistical uncertainty velocity values are estimated at  $\pm 0.20\text{m/s}$ .



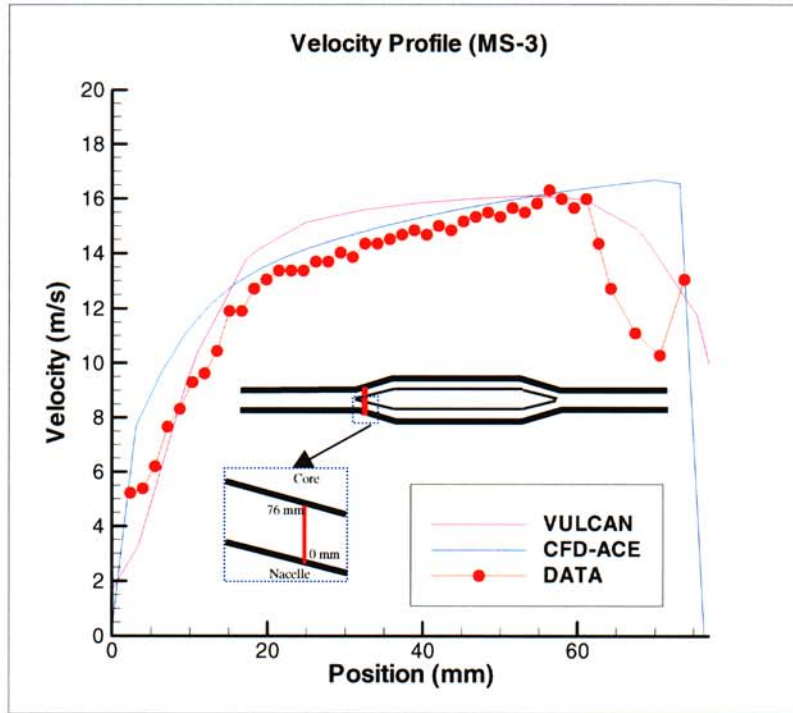


Figure 6.5 - Measurement Plane 3 Velocity Comparison

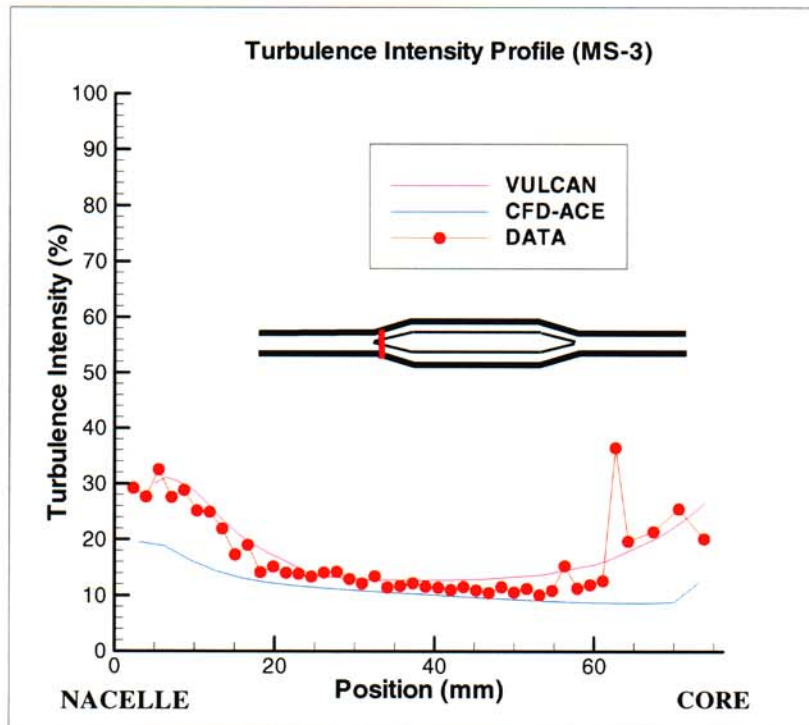


Figure 6.6 - Measurement Plane 3 Turbulence Intensity Comparison

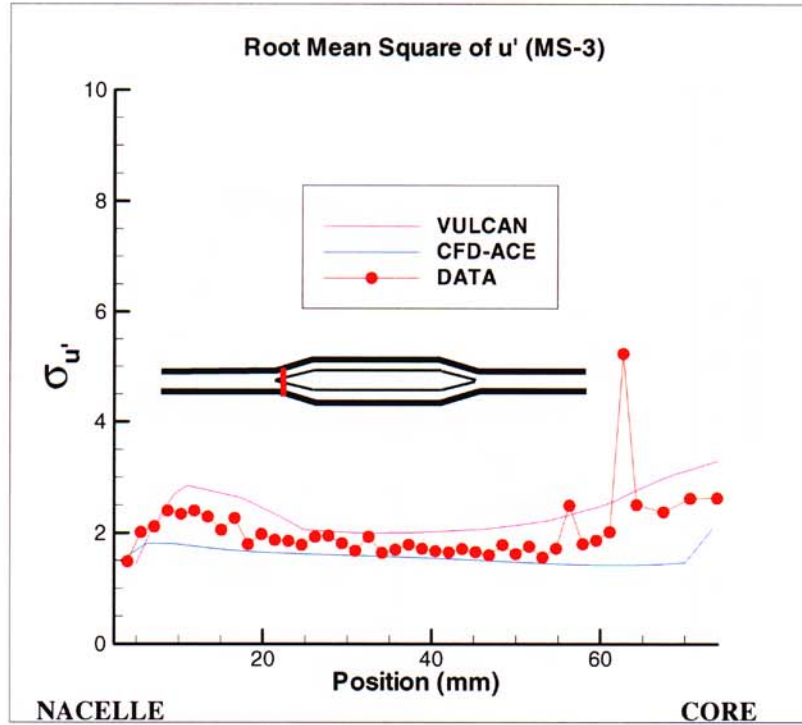


Figure 6.7 - Measurement Plane 3 Root Mean Square of  $u'_s$  Comparison

#### 6.4 Measurement Plane 4

Figures 6.8 and 6.9 show the velocity and turbulence intensity predicted by VULCAN and CFD-ACE at the second measurement plane (or mid-plane) in the transition region of the core. In Figure 6.8, the experimental velocities are higher than the CFD-ACE predictions, except near the core wall where the experimental data again drops off similar to measurement location 3 (Figure 6.5). In addition, there does appear to be some noise in the data near the nacelle wall; however, the measurement uncertainty associated with this noise is difficult to quantify. The VULCAN velocity predictions show a very narrow band of high velocity flow with rapid decreases in velocity away from the center of the channel. This feature is consistent with the VULCAN grid not being smooth along the angled walls which, in turn, is blocking more of the flow (see Figure 4.1). The experimental turbulence intensity values shown in Figure 6.9 are in agreement with the CFD predictions in the center of the channel but deviate near the walls. The largest difference in results occurs next to the nacelle wall in proportion to the difference in velocity shown in Figure 6.8. When the rms values of  $u'_s$  are plotted in Figure 6.10, the CFD predictions are in much better agreement with the experimental data. Statistical uncertainty in the measured mean velocity was estimated at  $\pm 0.20 \text{ m/s}$ .



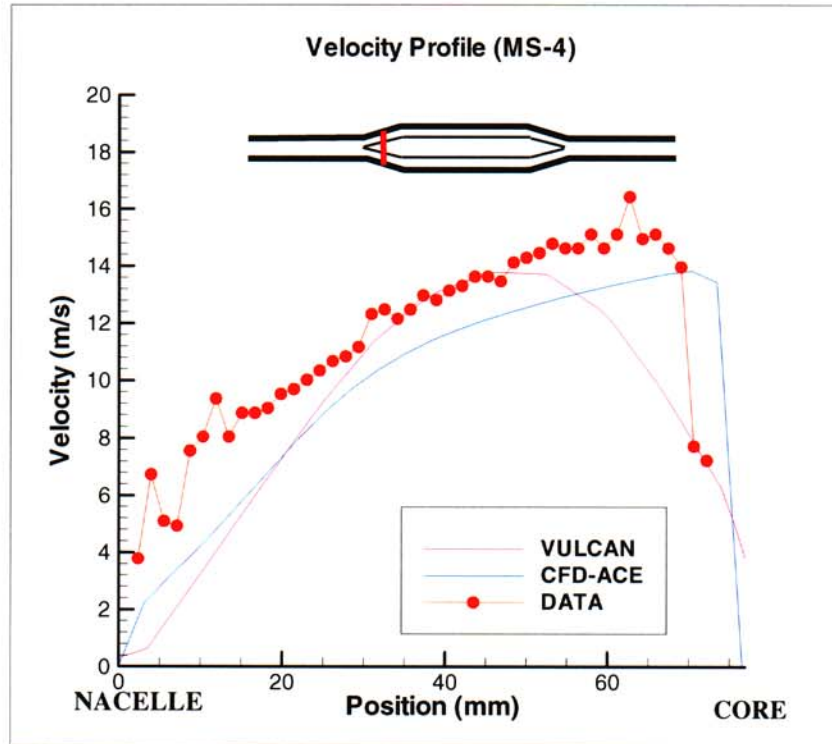


Figure 6.8 - Measurement Plane 4 Velocity Comparison

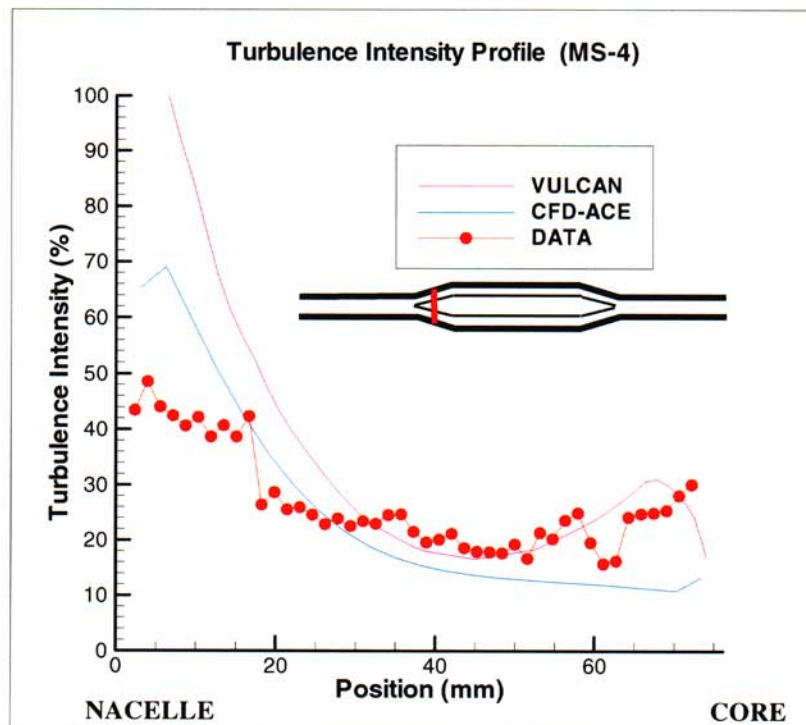


Figure 6.9 - Measurement Plane 4 Turbulence Intensity Comparison

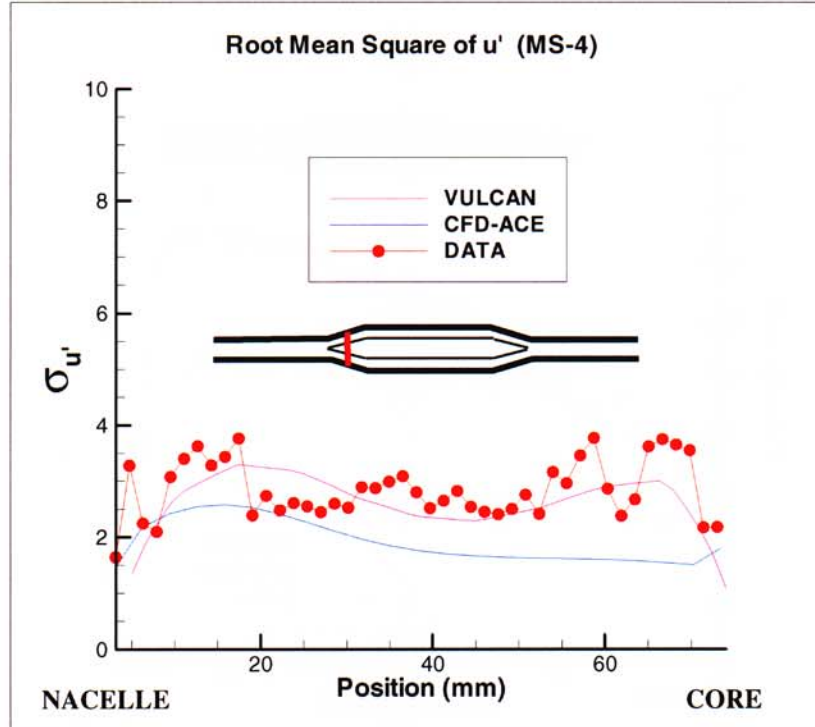


Figure 6.10 - Measurement Plane 4 Root Mean Square of  $u'_s$  Comparison

### 6.5 Measurement Plane 5

Figures 6.11 and 6.12 show the velocity and turbulence intensity predicted by VULCAN and CFD-ACE at the third measurement plane in the transition region of the core. At this location, the velocity results in Figure 6.11 show the same trend as the velocities at the previous measurement plane (MS-4). That is, the velocity results are similar in the center of the channel and deviate from each other near the walls. In Figure 6.12, CFD-ACE predicts very large turbulence intensity values near the nacelle wall with decreasing levels across the channel to the core wall. VULCAN predictions show large turbulence values near the nacelle wall, decreasing levels across the channel, and then a sudden increase in turbulence intensities near the core wall. This increase near the core wall could be attributed to the stair-stepped grid along the wall, which tends to reduce the streamwise flow and increase the cross-stream flow, thereby, causing higher turbulence levels. The experimental data show slightly higher values near the nacelle wall with decreasing values towards the core wall where some noise in the data is evident. The measurement uncertainty associated with the data near the wall is difficult to quantify. Again, these large differences between the CFD predictions and the experimental data near the nacelle wall can also be attributed in part to the differences in mean velocity. When the rms values of  $u'_s$  are plotted in



Figure 6.13, both code predictions are in much better agreement with the experimental data. Statistical uncertainty in the measured mean velocity was estimated at  $\pm 0.20\text{m/s}$ .

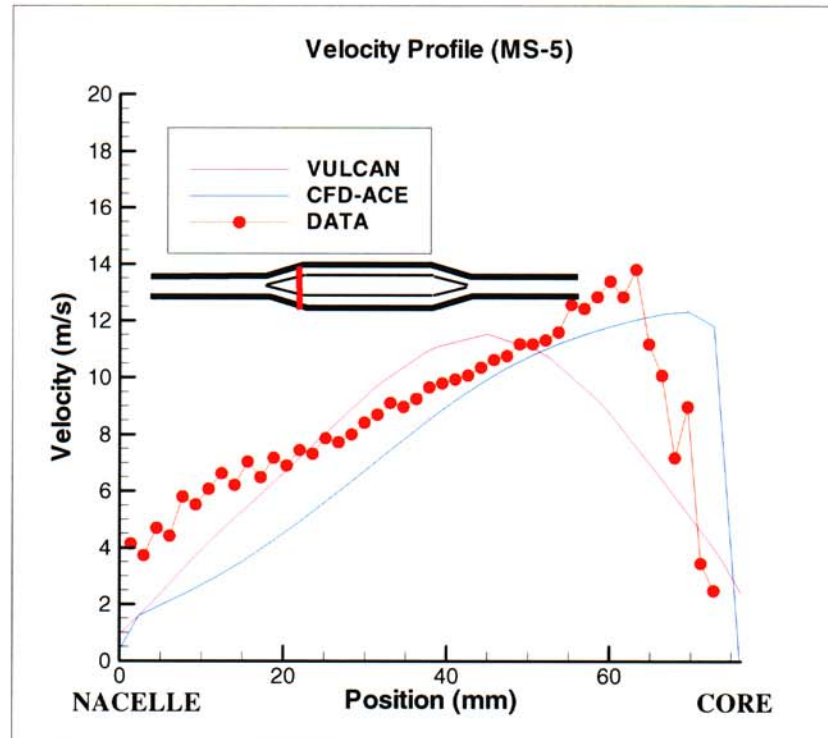


**Figure 6.11 - Measurement Plane 5 Velocity Comparison**

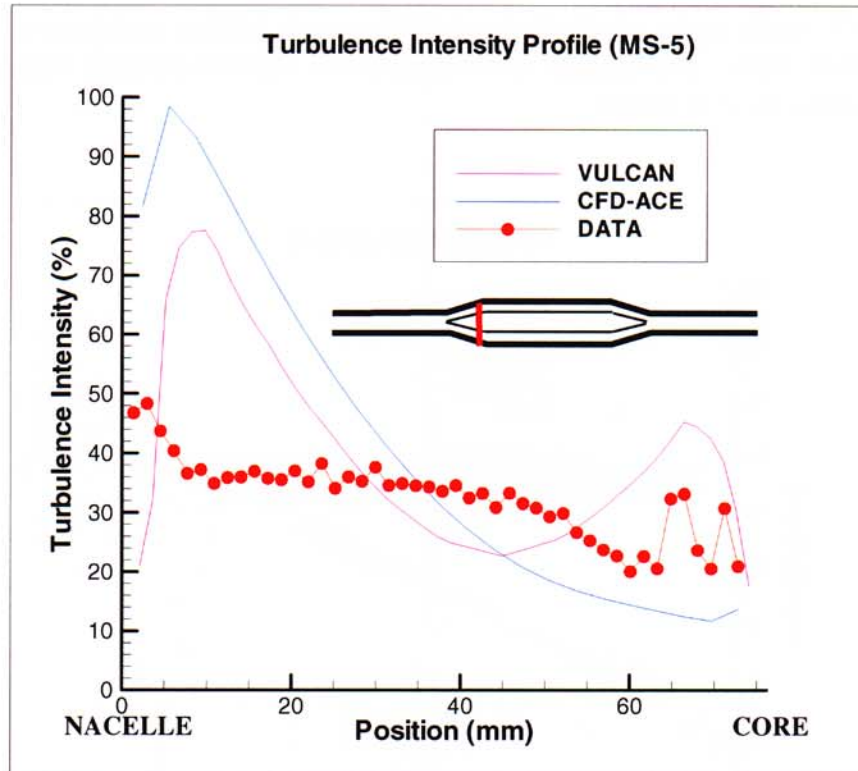


Figure 6.12 - Measurement Plane 5 Turbulence Intensity Comparison

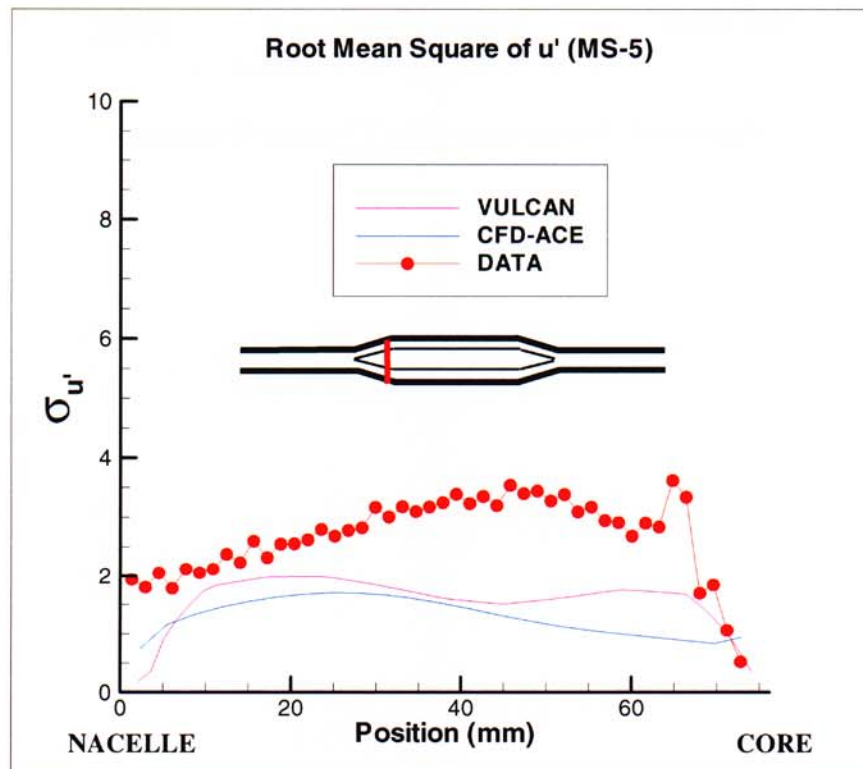


Figure 6.13 - Measurement Plane 5 Root Mean Square of  $u'_s$  Comparison



## 6.6 Measurement Plane 6

Figures 6.14 and 6.15 show the velocity and turbulence intensity predicted by VULCAN and CFD-ACE at the first measurement plane in the straight section of the core. In Figure 6.14, the experimental data show a much larger decrease in velocity than the CFD predictions. The maximum velocity observed in the experimental data decreased by approximately 7 m/s, the CFD-ACE prediction decreased by approximately 2 m/s, and the VULCAN prediction decreased by approximately 3 m/s from the previous measurement plane (MS-5). In addition, there does appear to be some noise in the data near the nacelle wall; however, the measurement uncertainty associated with this noise is difficult to quantify. Similar to measurement plane 5, the turbulence intensity values for CFD-ACE and VULCAN shown in Figure 6.15 are much larger than the experimental data near the nacelle wall. In addition, the experimental data contains a lot of noise, especially near the nacelle wall. When the rms values of  $u'_s$  are plotted in Figure 6.16, the CFD predictions are in much better agreement with the experimental data. Statistical uncertainty in the measured mean velocity was estimated at  $\pm 0.22$  m/s.

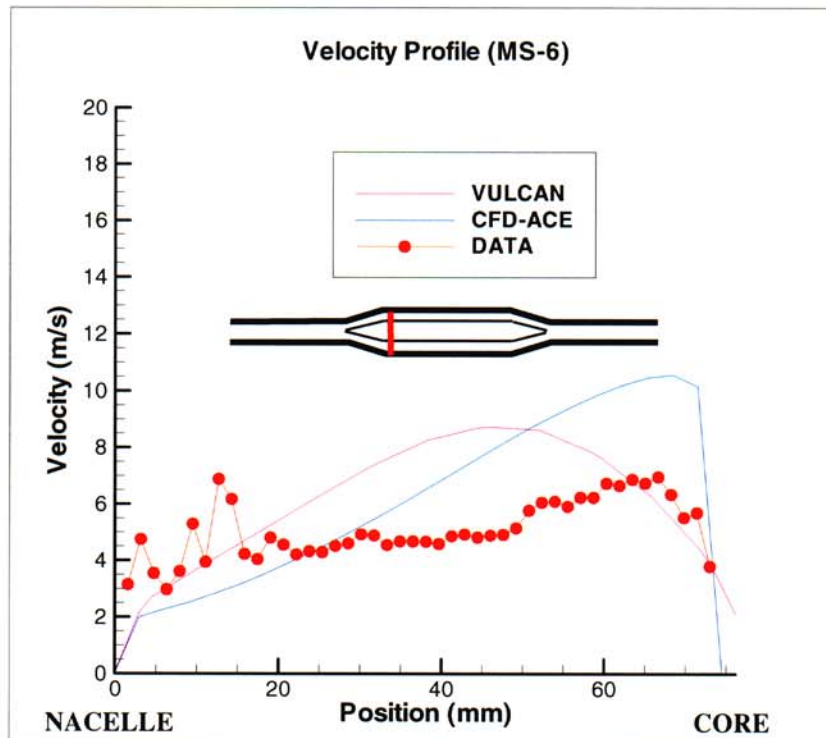


Figure 6.14 - Measurement Plane 6 Velocity Comparison

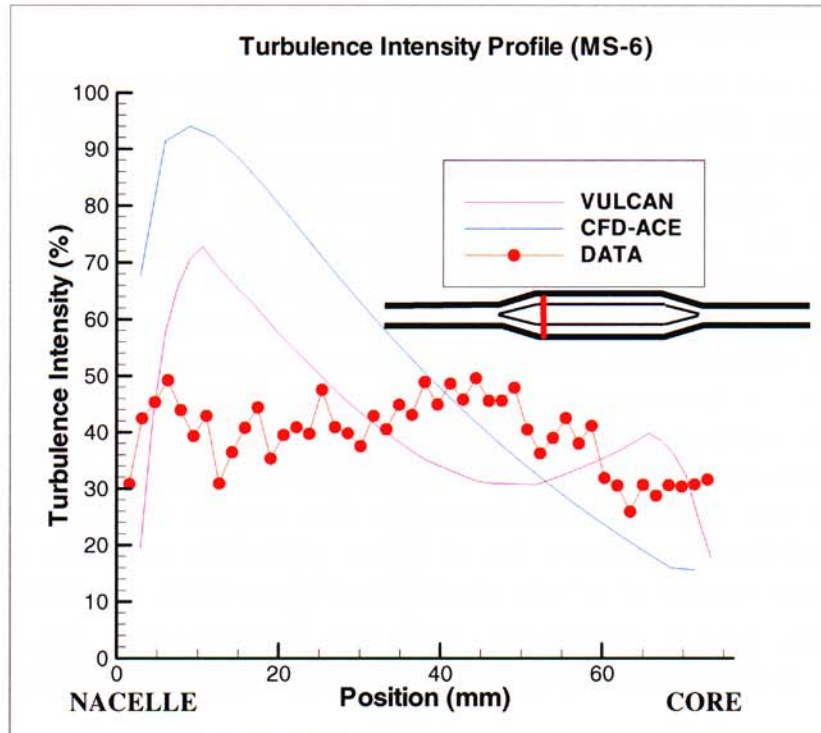


Figure 6.15 - Measurement Plane 6 Turbulence Intensity Comparison

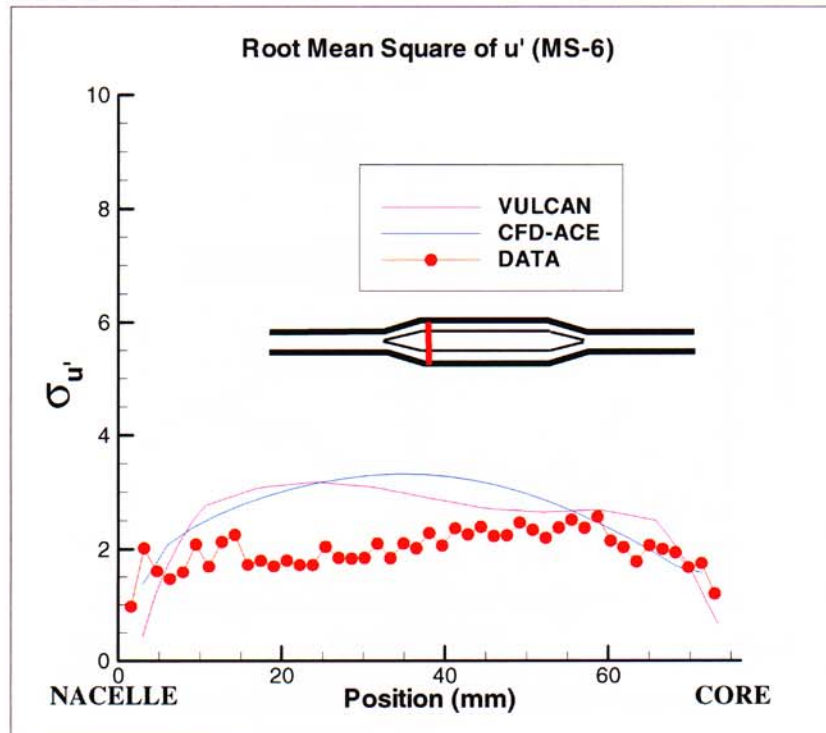


Figure 6.16 - Measurement Plane 6 Root Mean Square of  $u'_s$  Comparison



## 6.7 Measurement Plane 7

Figures 6.17 and 6.18 show the velocity and turbulence intensity predicted by VULCAN and CFD-ACE at the second measurement plane (or mid-plane) in the straight section of the core. At this location, the velocity predictions shown in Figure 6.16 are in very good agreement with the experimental data. Any misalignment between the core and the flow direction would be minimized at this location. In Figure 6.18, the CFD predictions of turbulence intensities show reasonable agreement with the data. Near the walls, the data show both larger turbulence intensity values and higher levels of noise. It should be noted that the experimental data at this measurement station (and at MS-8 and MS-9) does not span the entire distance to the core wall. Statistical uncertainty in the measured mean velocity was estimated at  $\pm 0.22\text{m/s}$ .

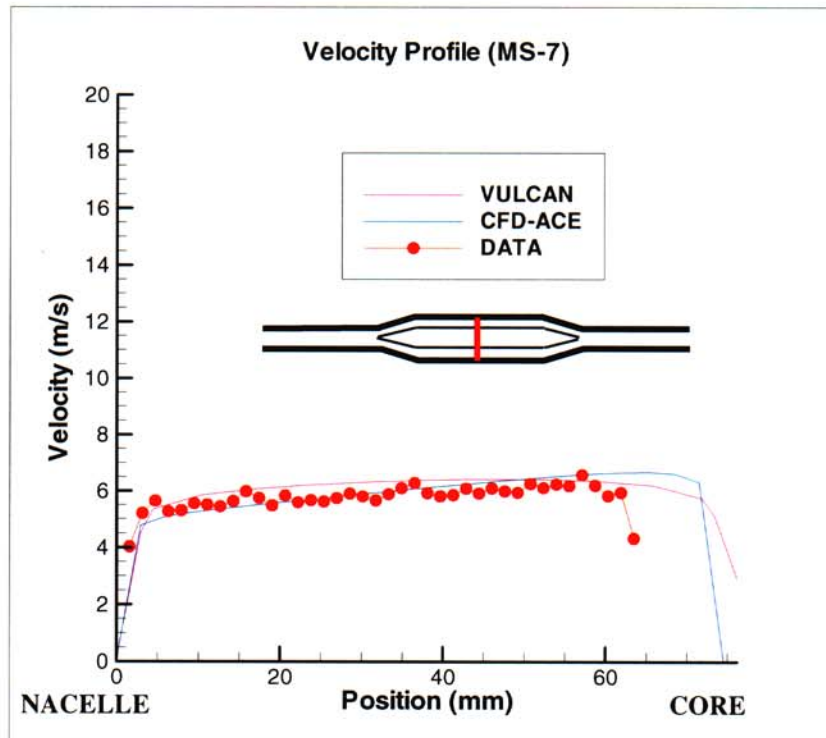


Figure 6.17 - Measurement Plane 7 Velocity Comparison

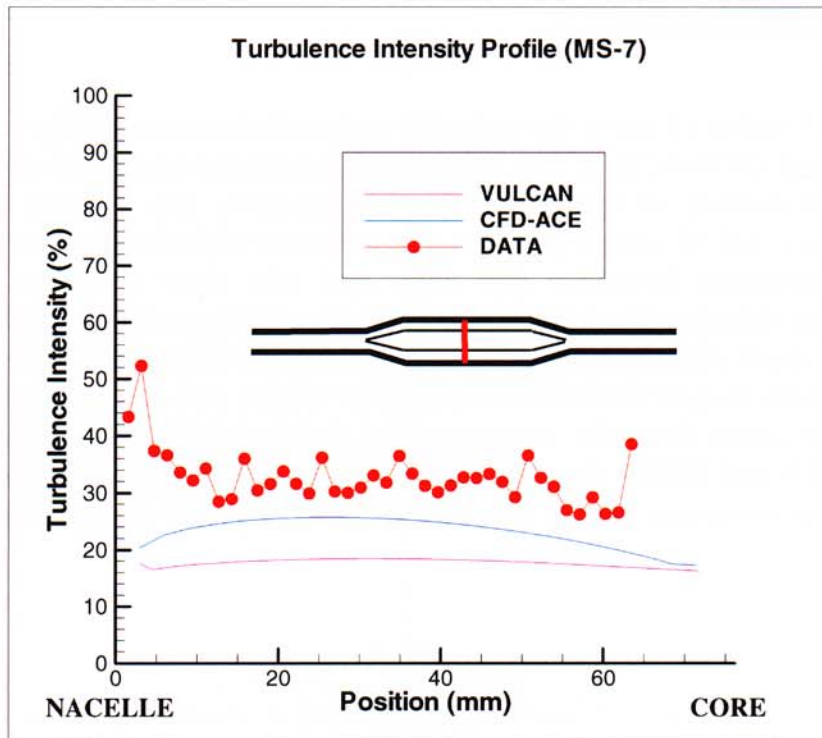


Figure 6.18 - Measurement Plane 7 Turbulence Intensity Comparison

## 6.8 Measurement Plane 8

Figures 6.19 and 6.20 show the velocity and turbulence intensity predicted by VULCAN and CFD-ACE at the third (and final) measurement plane in the straight section of the core. The velocity predictions shown in Figure 6.19 are in reasonable agreement with the experimental data. The experimental velocities, which were level at measurement station 7 (Figure 6.17), are slightly lower in the center of the channel. The turbulence intensity values for CFD-ACE and VULCAN are in good agreement with each other but are roughly 10% less than the experimental data as shown in Figure 6.20. Statistical uncertainty in the measured mean velocity was estimated at  $\pm 0.22\text{m/s}$ .



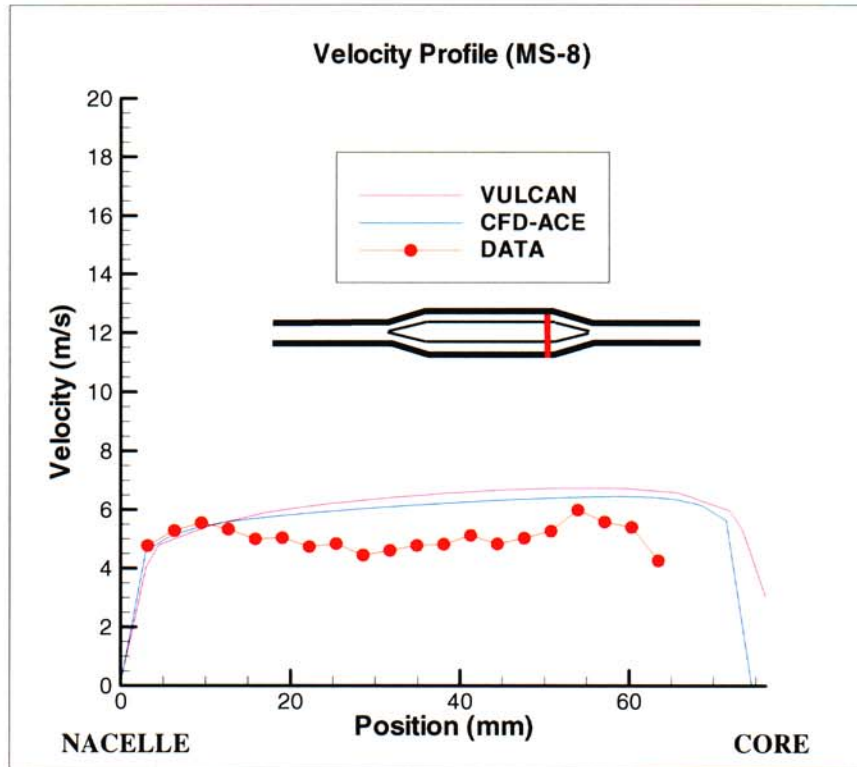


Figure 6.19 - Measurement Plane 8 Velocity Comparison

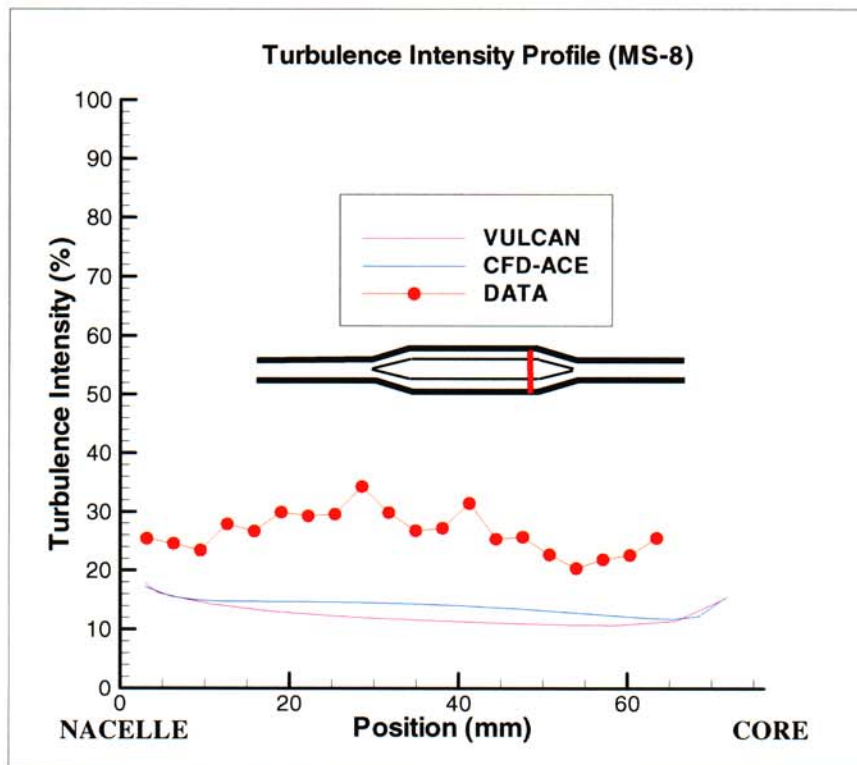


Figure 6.20 - Measurement Plane 8 Turbulence Intensity Comparison

## 6.9 Measurement Plane 9

Figures 6.21 and 6.22 show the velocity and turbulence intensity predicted by VULCAN and CFD-ACE at a measurement plane centered in the rear transition region of the core. The CFD-ACE velocity predictions shown in Figure 6.21 are in very good agreement with the experimental data; whereas, the VULCAN predictions show the flow velocity decreasing near both walls and increasing in the center of the channel. This feature is due to the stair-stepped grid along the angled walls, which tends to direct the flow into center of the channel. In Figure 6.22, both CFD-ACE and VULCAN predict approximately 10% lower turbulence intensity values than the experimental data, similar to the previous measurement plane (MS-8). At this location, two different experimental data sets (DATA and DATA2) were included so that an assessment of the repeatability of the tests could be made. Notice that DATA2 does not include the region near the nacelle wall where high noise in the data exist. Statistical uncertainty in the measured mean velocity was estimated at  $\pm 0.20\text{m/s}$ .

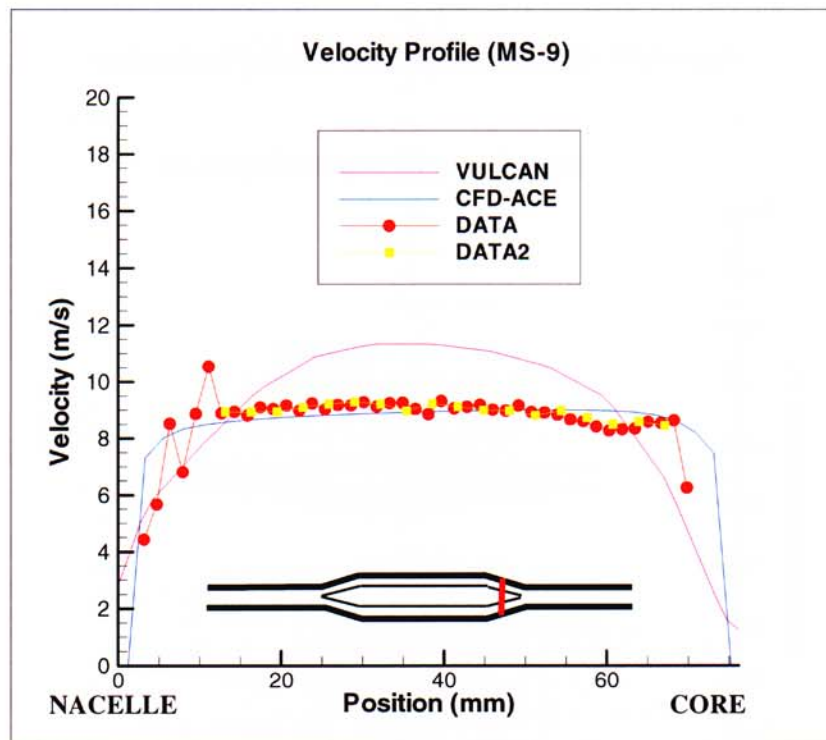


Figure 6.21- Measurement Plane 9 Velocity Comparison



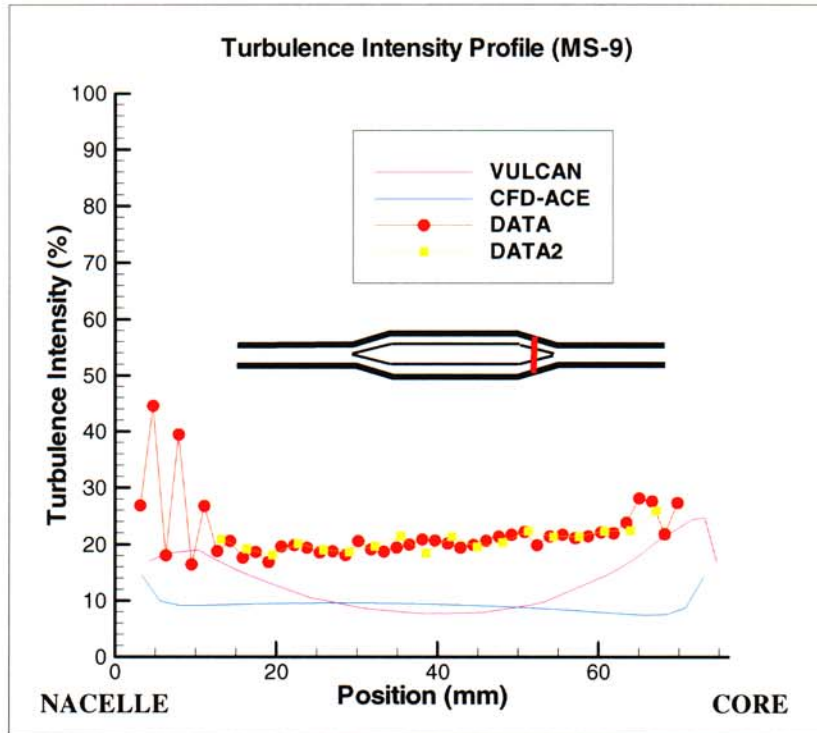


Figure 6.22 - Measurement Plane 9 Turbulence Intensity Comparison

### 6.10 Measurement Plane 10

Figures 6.23 and 6.24 show the velocity and turbulence intensity profiles predicted by VULCAN and CFD-ACE at the first measurement plane in the outlet section. The CFD-ACE velocity predictions at this location shown in Figure 6.23 are in very good agreement with the experimental data. It is speculated that there is a wake behind the core, which causes reduced axial velocities near the center of the pipe. While the VULCAN predictions show a similar trend in its velocity profile, the effect of the stair-stepped grid in the previous measurement station (MS-9) appears to still be noticeable at this location, even though the walls are no longer angled. In Figure 6.24, all of the turbulence intensity values are in the same range. Both CFD predictions show the effect of the wake flow on the turbulence intensity values in the center of the pipe; whereas, the experimental data values do not resolve this feature.

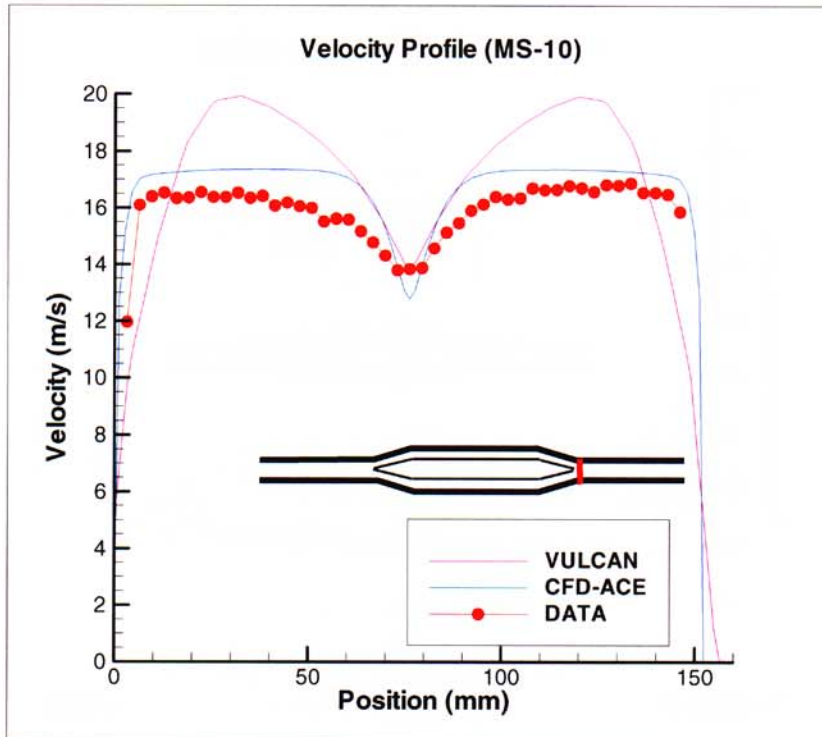


Figure 6.23 - Measurement Plane 10 Velocity Comparison

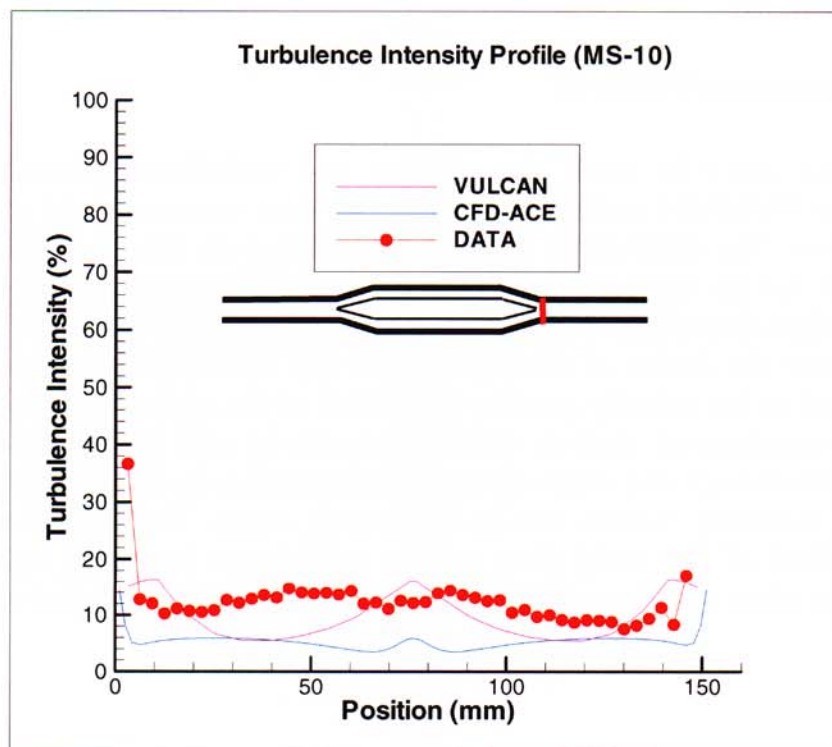


Figure 6.24 - Measurement Plane 10 Turbulence Intensity Comparison



## 6.11 Measurement Plane 11

Figures 6.25 and 6.26 show the velocity and turbulence intensity predicted by VULCAN and CFD-ACE at the final measurement plane in the outlet section. In Figure 6.25, the predicted velocity profiles show the wake diminishing with increasing distance from the core. The experimental data do not illustrate the presence of a wake region and in addition, appear to contain increased noise levels. There are noticeably fewer data points across the diameter of the pipe. The turbulence intensity values measured in the experiment are considerably higher than the CFD predictions as shown in Figure 6.26. In addition, the experimental values have increased by a factor of three from the previous measurement location (MS-10). CFD-ACE predicts constant turbulence intensity values below 10% for the majority of the flow across the pipe.

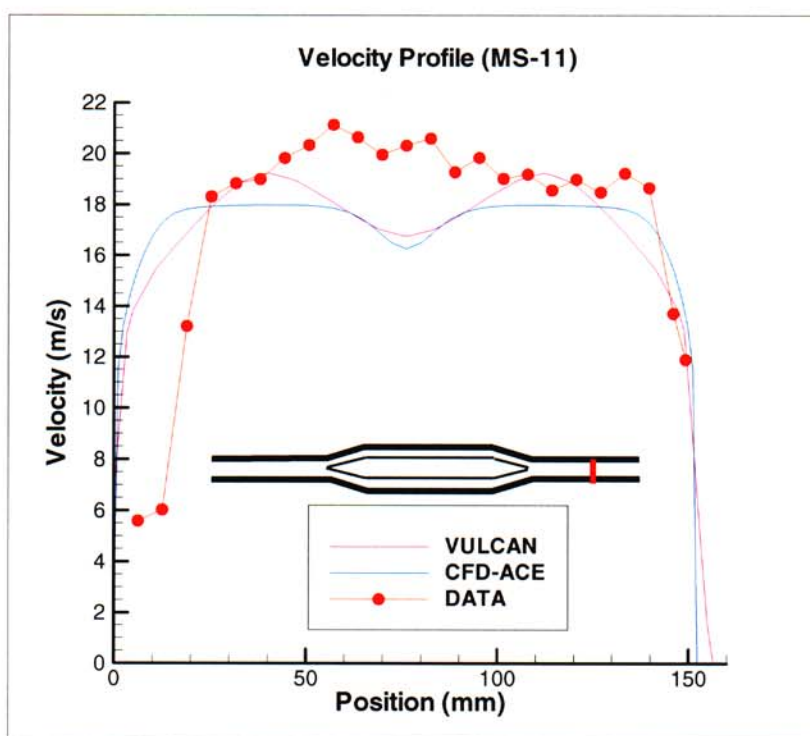
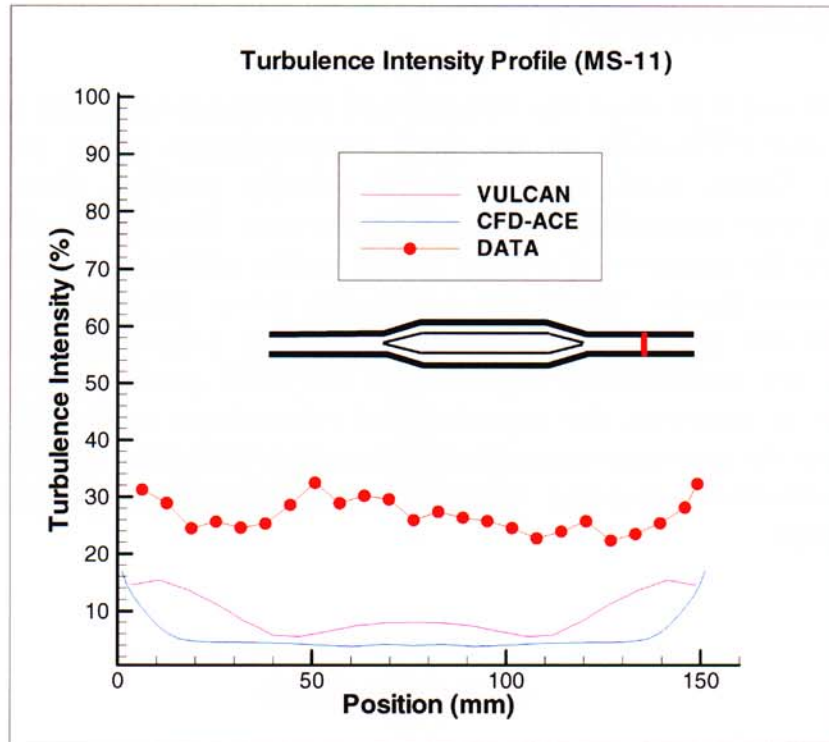


Figure 6.25 - Measurement Plane 11 Velocity Comparison



**Figure 6.26 - Measurement Plane 11 Turbulence Intensity Comparison**



## 7. Sensitivity Study

Three different sets of simulations using CFD-ACE were performed to assess the sensitivity of the results to the grid size and the turbulence models. In the first simulation, the coarsened computational grid, with 47,112 grid points, was used with the same turbulent kinetic energy relation used in the original set of calculations. In the second simulation, the isotropic turbulent flow assumption was used with the fine mesh. The results of both simulations (ACE-Coarse and ACE-Turbulence) were compared to the original CFD-ACE solution and the experimental data. Comparisons are shown at only four measurement planes for the ACE-Coarse solution and at every other measurement plane for the ACE-Turbulence solution. In the third set of simulations, two calculations were performed, one with the  $k-\omega$  (ACE-KOMEGA) turbulence model and the other with the Low Reynolds Number  $k-\epsilon$  (ACE-LRE) turbulence model, to investigate the effect of wall functions on the solution. In order to reduce computational time, a 2-D axisymmetric calculation was performed and compared to the 3-D solution and the results were identical. Therefore, the  $k-\omega$  and low Reynolds number calculations were performed using a 2-D fine mesh with 301 axial points and 150 radial points, which resulted in a nominal  $y^+$  value of 0.3. Both turbulence model results were compared to the original CFD-ACE solution and the experimental data at measurement location 3.

### 7.1 Coarse Grid Results

Figures 7.1 and 7.2 show the specified velocity and turbulence intensity for the coarse grid solution (ACE-Coarse) at the inlet plane (MS-1) of the calculation. It should be noted that the velocity and turbulence intensity scales have been reduced from the previous comparisons in order to highlight the differences in the solutions. In both figures, the ACE-Coarse solution follows the fit of the experimental data (and the CFD-ACE solution), except in the center of the pipe where the decreased grid resolution produces a slight deviation from the input values.

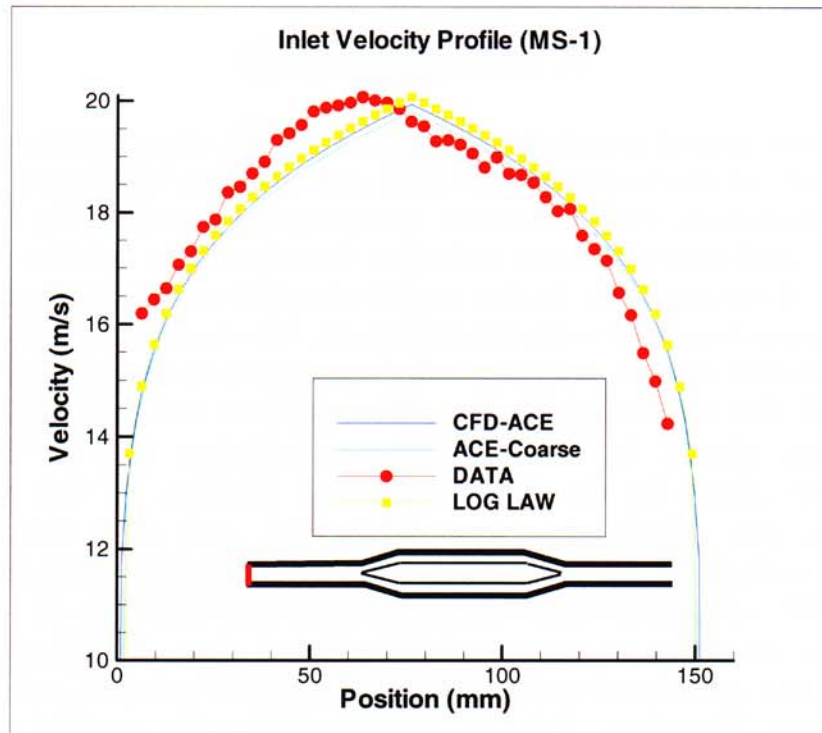


Figure 7.1 - Grid Sensitivity: Measurement Plane 1 Velocity Comparison

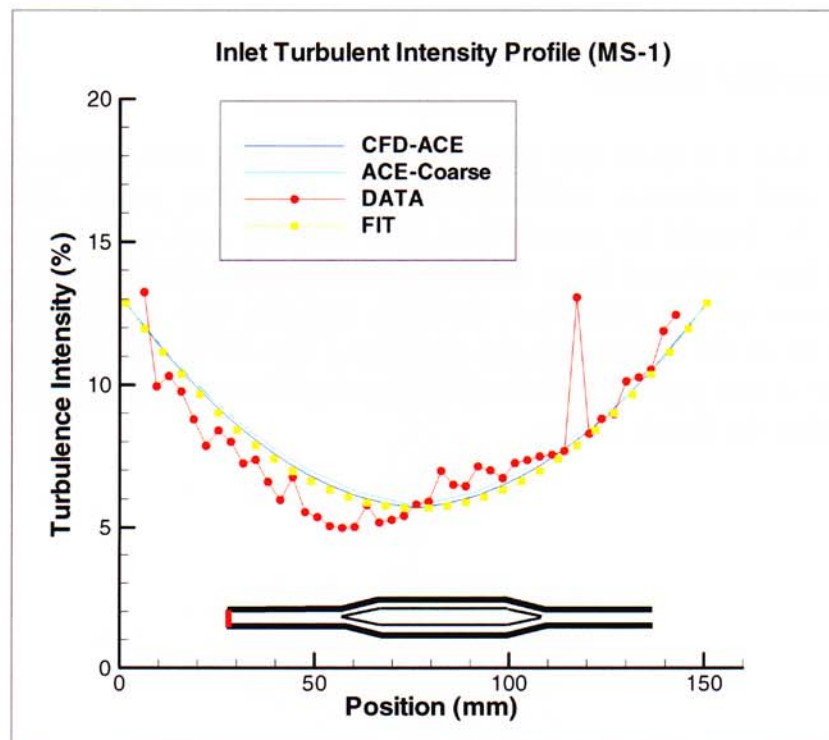


Figure 7.2 - Grid Sensitivity: Measurement Plane 1 Turbulence Intensity Comparison



Figures 7.3 and 7.4 show the predicted velocity and turbulence intensity for ACE-Coarse at the first measurement plane in the transition region of the core. In both figures, the ACE-Coarse solution matches the CFD-ACE solution, except in the near wall regions. Again, this difference results from the lack of grid resolution near the nacelle and core walls in the coarse grid solution.

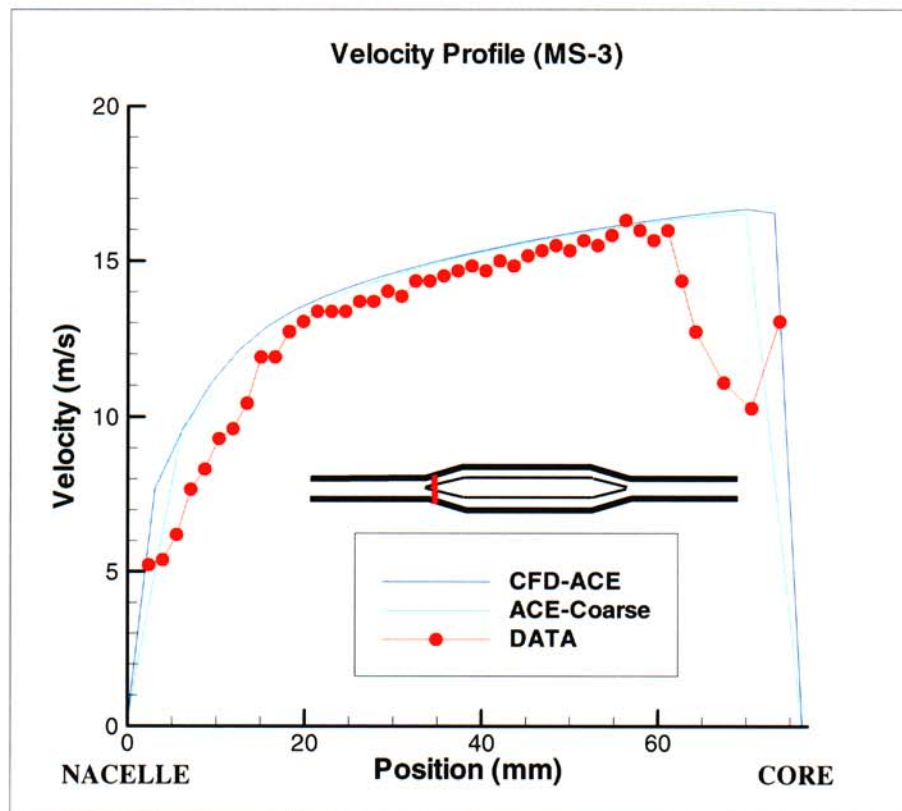
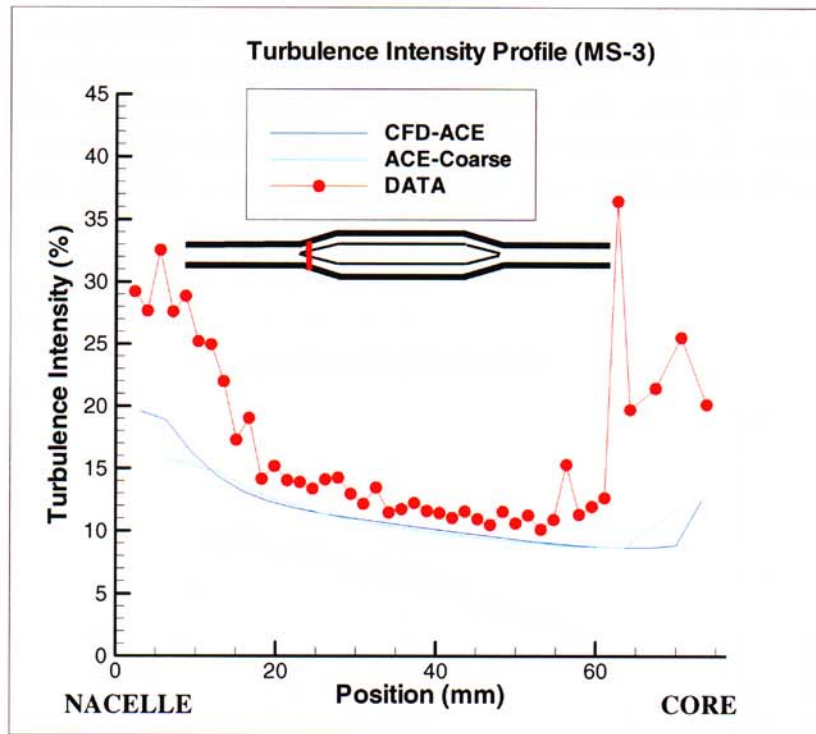


Figure 7.3 - Grid Sensitivity: Measurement Plane 3 Velocity Comparison



**Figure 7.4 - Grid Sensitivity: Measurement Plane 3 Turbulence Intensity Comparison**

Figures 7.5 and 7.6 show the predicted velocity and turbulence intensity for ACE-Coarse at the second measurement plane (or mid-plane) in the straight section of the core. Similar to measurement plane 5, the ACE-Coarse velocity prediction (in Figure 7.5) matches the CFD-ACE solution, except in the near wall regions. In Figure 7.6, the ACE-Coarse turbulence intensity prediction shows good agreement with the CFD-ACE solution.

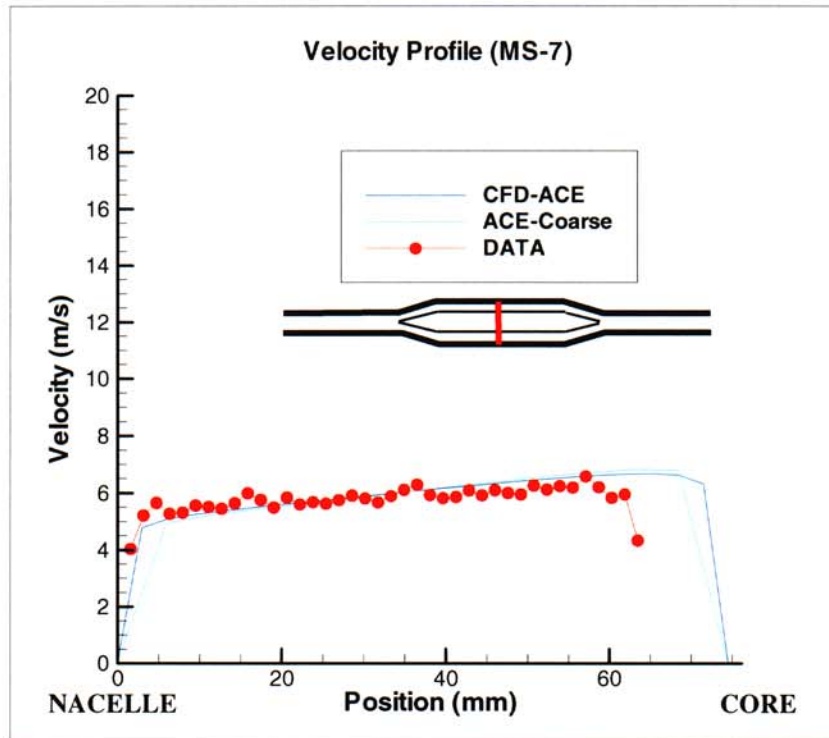


Figure 7.5 - Grid Sensitivity: Measurement Plane 7 Velocity Comparison

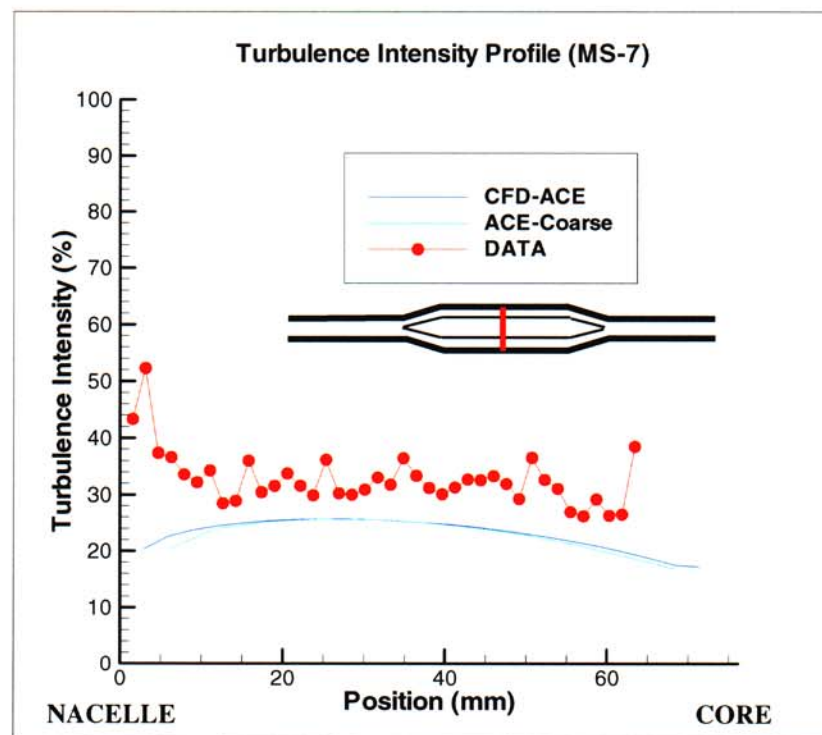


Figure 7.6 - Grid Sensitivity: Measurement Plane 7 Turbulence Intensity Comparison



Figures 7.7 and 7.8 show the predicted velocity and turbulence intensity for ACE-Coarse at the final measurement plane in the outlet pipe. The ACE-Coarse velocities and turbulence intensities compare well with the CFD-ACE solution. Small deviations in ACE-Coarse results are shown near the center of pipe due to poorer grid resolution of the wake flow region behind the core.

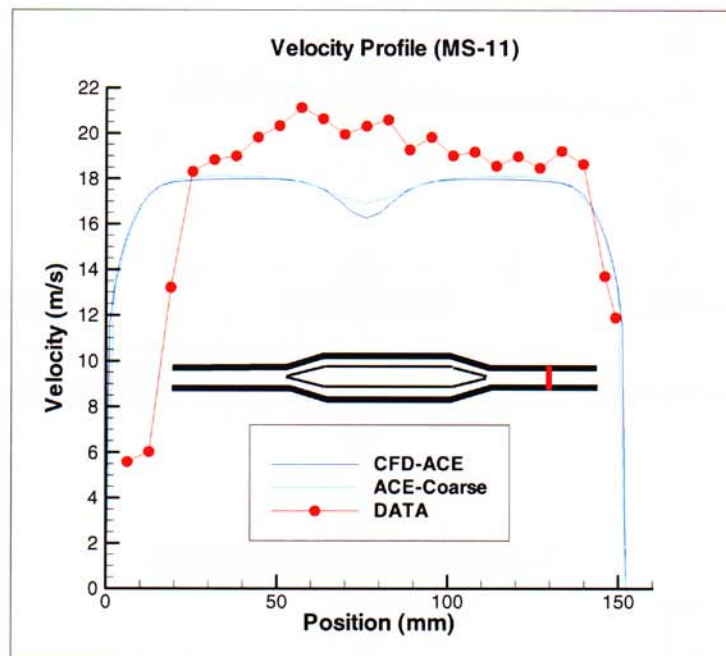


Figure 7.7 - Grid Sensitivity: Measurement Plane 11 Velocity Comparison

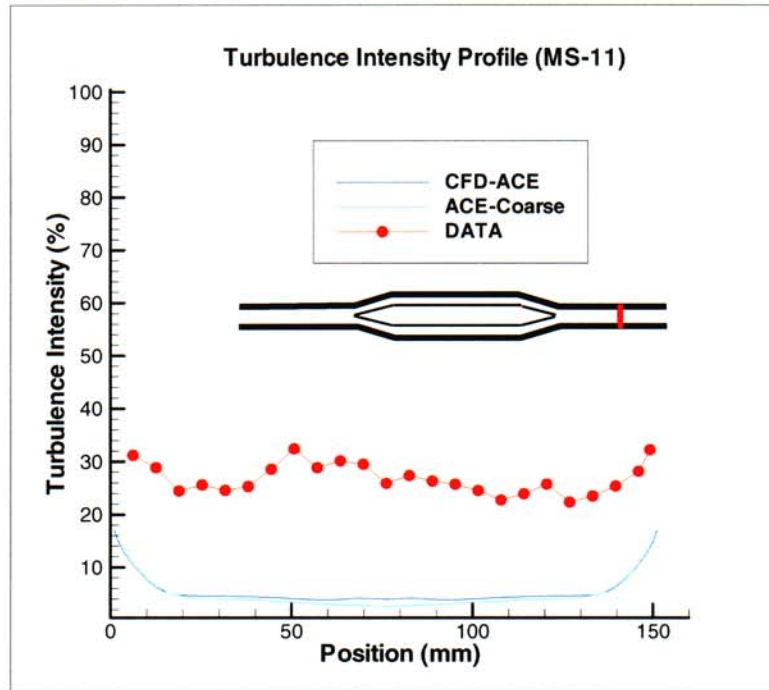


Figure 7.8 - Grid Sensitivity: Measurement Plane 11 Turbulence Intensity Comparison

Overall the coarse mesh solution (ACE-Coarse) showed good agreement with the fine mesh solution (CFD-ACE). Some differences occurred near wall regions due to the lack of grid resolution.

## 7.2 Isotropic Turbulence Model Results

As expected, the predicted velocity and turbulence intensity using the isotropic turbulence relation (ACE-Turbulence) exactly match the original CFD-ACE solution at the inlet plane (MS-1) of the calculation; therefore, these plots will not be shown here.

Figures 7.9 and 7.10 show the predicted velocity and turbulence intensity for the ACE-Turbulence solution at the first measurement plane in the transition region of the core. The ACE-Turbulence velocity prediction (Figure 7.9) is slightly higher near the nacelle wall and slightly lower near the core wall than the CFD-ACE velocity prediction. In Figure 7.10, the ACE-Turbulence prediction is consistently lower than the CFD-ACE turbulence intensity result, and even up to 50% different next to the nacelle wall.

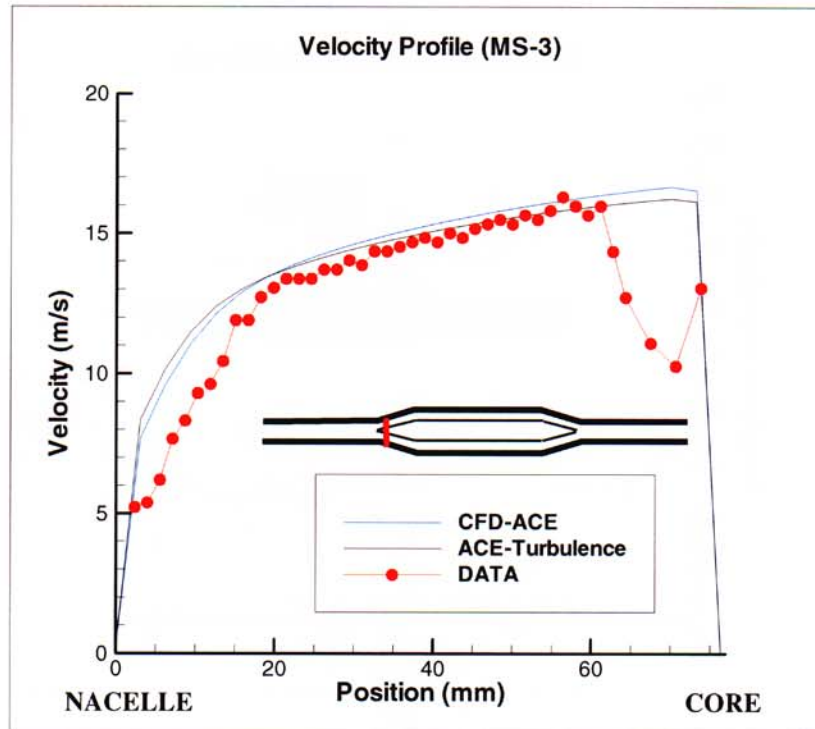


Figure 7.9 - Isotropic Turbulent Flow: Measurement Plane 3 Velocity Comparison

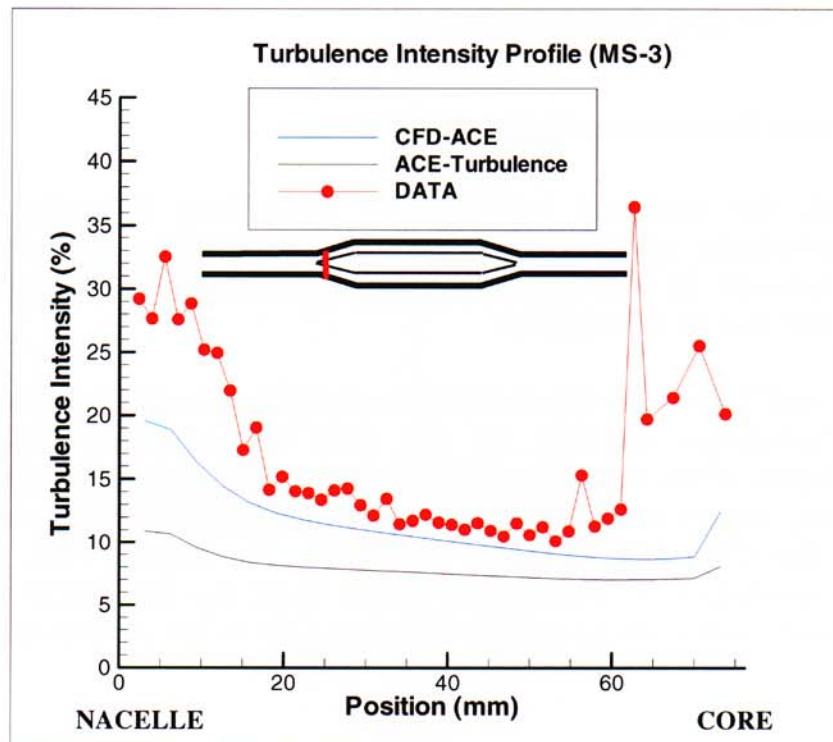
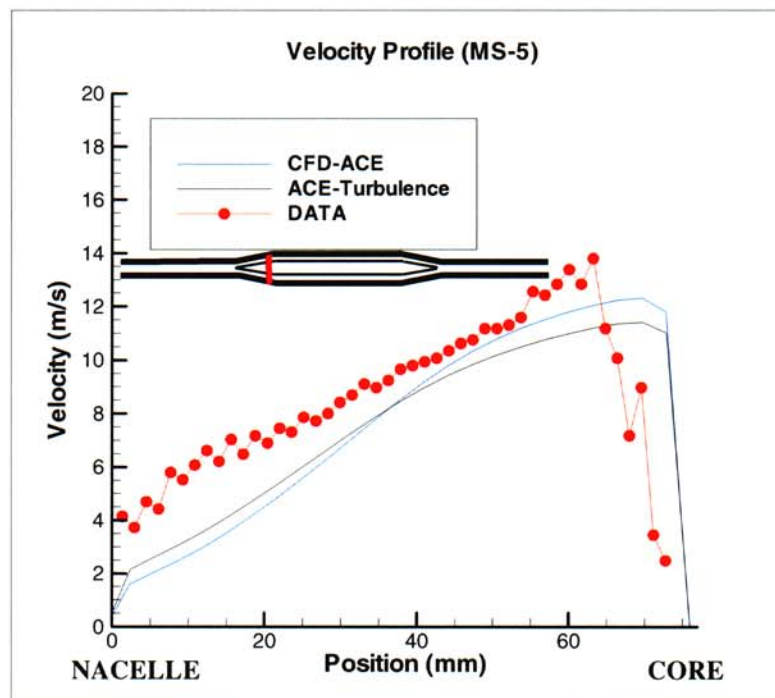


Figure 7.10 - Isotropic Turbulent Flow: Measurement Plane 3 Turbulence Intensity Comparison



Figures 7.11 and 7.12 show the predicted velocity and turbulence intensity for the ACE-Turbulence solution at the third measurement plane in the transition region of the core. Again, the ACE-Turbulence velocity prediction (Figure 7.11) is slightly higher near the nacelle wall and lower near the core wall relative to the CFD-ACE result. Notice that the difference in velocity between the predictions has doubled from the difference in measurement plane 3. In Figure 7.12, both of the predicted turbulence intensity values have increased by a factor of approximately 5 near the nacelle wall. Again, the turbulence intensity values for ACE-Turbulence result are less than the CFD-ACE result and both results are noticeably different than the experimental data at this location.



**Figure 7.11 - Isotropic Turbulent Flow: Measurement Plane 5 Velocity Comparison**

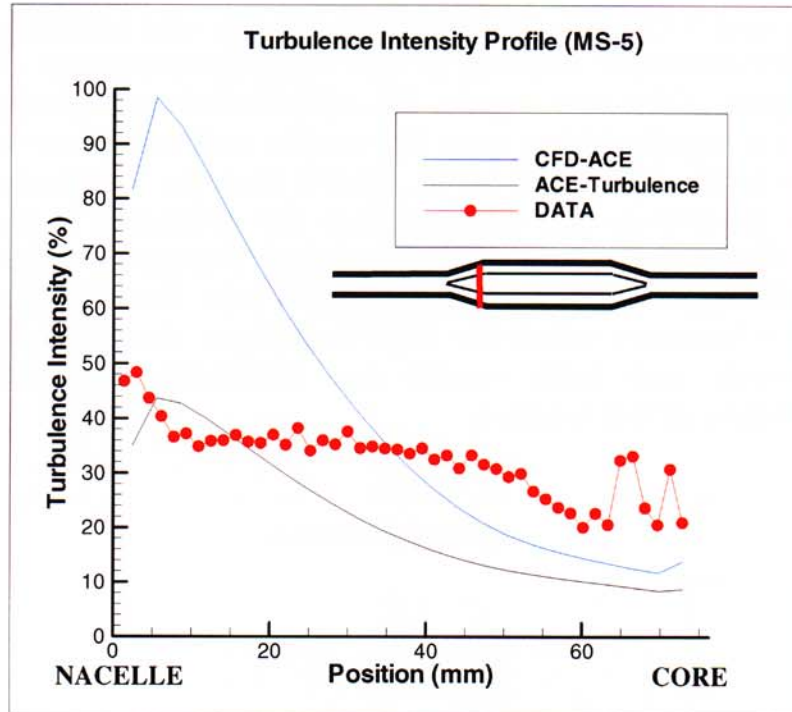


**Figure 7.12 - Isotropic Turbulent Flow: Measurement Plane 5 Turbulence Intensity Comparison**

Figures 7.13 and 7.14 show the predicted velocity and turbulence intensity for the ACE-Turbulence solution at the second measurement plane (or mid-plane) in the straight section of the core. At this location, the ACE-Turbulence velocity prediction (Figure 7.13) shows very good agreement with the CFD-ACE solution and the experimental data. However, the CFD-Turbulence turbulence intensity result shown in Figure 7.14 is roughly half the value of the CFD-ACE result and significantly different from the experimental data.

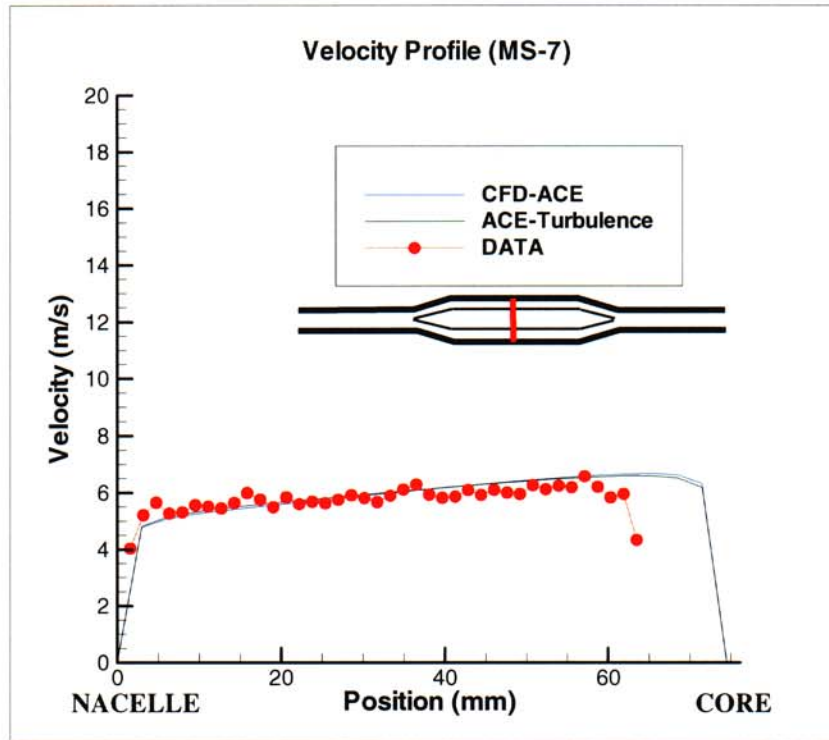


Figure 7.13 - Isotropic Turbulent Flow: Measurement Plane 7 Velocity Comparison

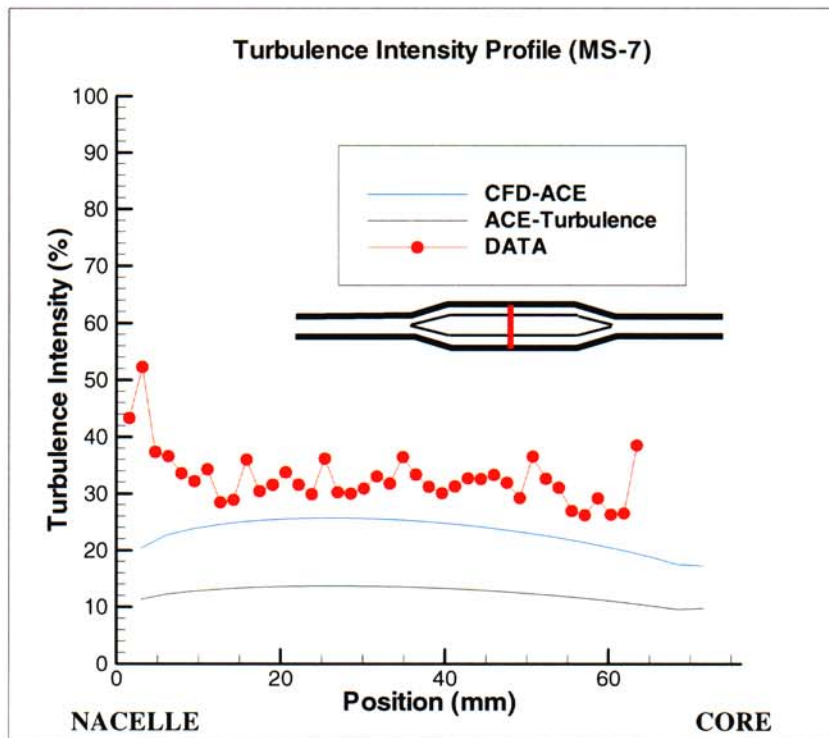


Figure 7.14 - Isotropic Turbulent Flow: Measurement Plane 7 Turbulence Intensity Comparison



Figures 7.15 and 7.16 show the predicted velocity and turbulence intensity for the ACE-Turbulence solution at a measurement plane centered in the rear transition region of the core. Similar to measurement station 7, the ACE-Turbulence velocity result (Figure 7.15) shows very good agreement with the CFD-ACE solution and the experimental data. However, the ACE-Turbulence result shown in Figure 7.16 underpredicts the turbulence intensities by a larger amount than the CFD-ACE solution.

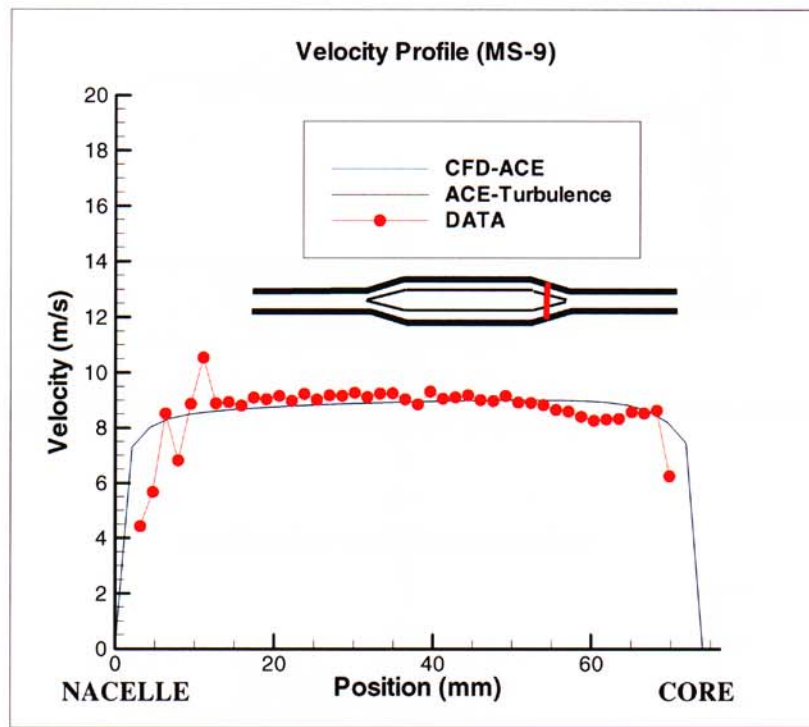
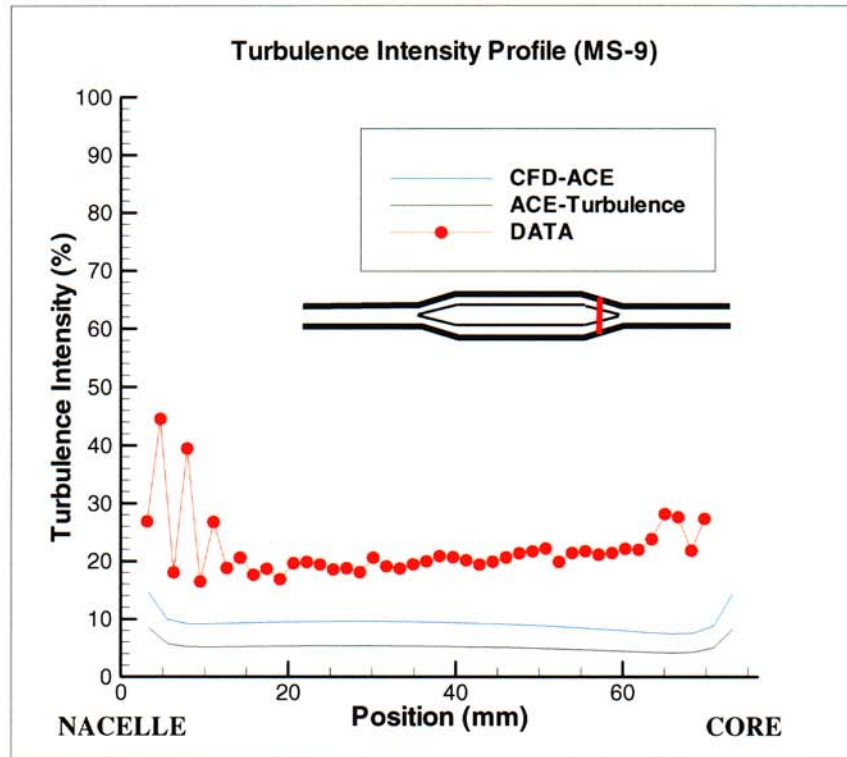


Figure 7.15 - Isotropic Turbulent Flow: Measurement Plane 9 Velocity Comparison



**Figure 7.16 - Isotropic Turbulent Flow: Measurement Plane 9 Turbulence Intensity Comparison**

Figures 7.17 and 7.18 show the predicted velocity and turbulence intensity for the ACE-Turbulence solution at the final measurement plane in the outlet pipe. The ACE-Turbulence velocity prediction (in Figure 7.17) is slightly less than the CFD-ACE solution, except near the walls where it is higher and in the wake region where the assumption of turbulent isotropic flow tends to intensify the effect of the core on the flow. In Figure 7.18, the ACE-Turbulence turbulence intensities are less than the CFD-ACE result and the experimental data.

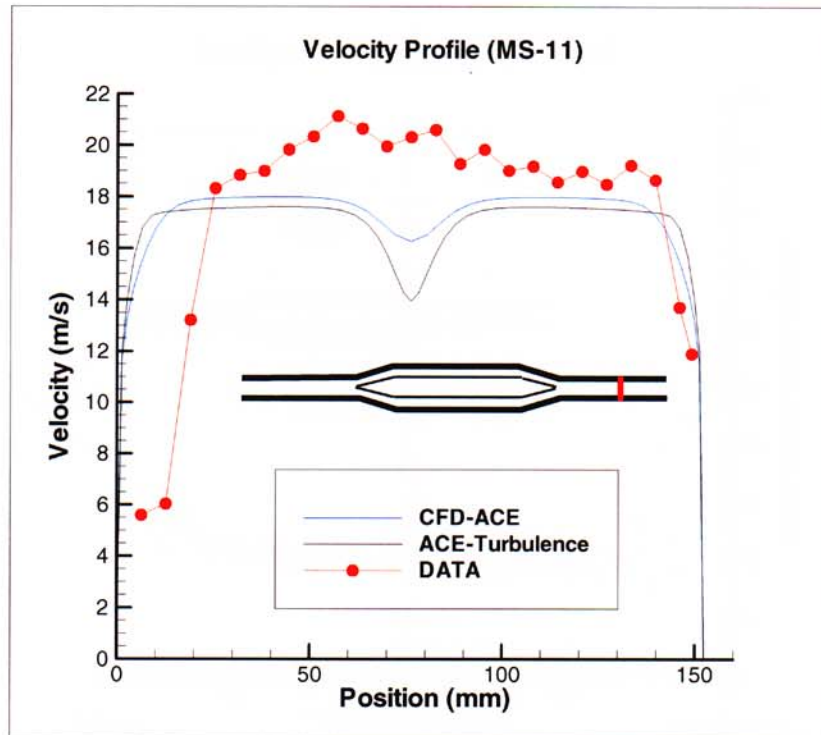


Figure 7.17 - Isotropic Turbulent Flow: Measurement Plane 11 Velocity Comparison

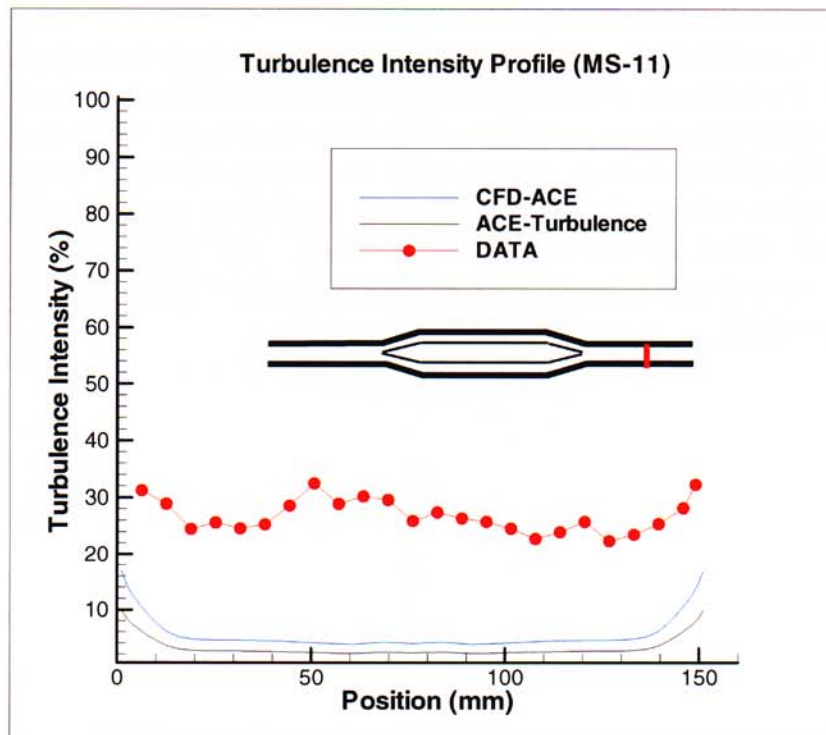


Figure 7.18 - Isotropic Turbulent Flow: Measurement Plane 11 Turbulence Intensity Comparisons



Overall the assumption of zero cross-stream turbulent velocity results showed better agreement with the experimental data than the isotropic turbulent flow assumption. Therefore for this problem, it is best not to assume that the turbulent flow is isotropic.

### **7.3 *k- $\omega$ and Low Reynolds Number Turbulence Model Results***

At measurement location 3 (Figure 6.5), large differences in velocity results occurred between the CFD-ACE solution and the experimental data near the core wall. A numerical study was performed to determine if the wall functions used in the CFD-ACE solution failed to capture the velocity dip near the core wall. It is well known that wall functions fail in regions where large adverse pressure gradients exist and for this case, the majority of the inlet transition duct did contain an adverse pressure gradient. For both turbulence model cases, a 2-D axisymmetric calculation was performed using the same number of grid points (301) as the fine mesh in the axial direction. In the radial direction, the number of grid points was increased from 25 to 150 so that a nominal  $y^+$  value of 0.3 was achieved at the first grid point away from both the nacelle wall and the core wall.

Figures 7.19 and 7.20 show the predicted velocity and turbulence intensity profiles for both the ACE-KOMEGA and ACE-LRE solutions at the first measurement plane in the transition region of the core. The ACE-KOMEGA velocity profile, shown in Figure 7.19, is very similar to the ACE-LRE solution. In addition, these solutions are consistent with the CFD-ACE solution in that they do not predict a velocity dip near the core wall. As expected, slight differences did occur near both walls due to the use of wall functions in the CFD-ACE solution. In Figure 7.20, the turbulent intensity values for the ACE-KOMEGA solution and the ACE-LRE solution differ slightly near the walls. In addition, both solutions predict lower turbulence intensity values than the experimental data near the core wall. A better comparison can be made by plotting the rms value of  $u'_s$ , as shown in Figure 7.21. In this figure, both the ACE-KOMEGA solution and the ACE-LRE solution show slightly better agreement with the experimental data, except near the core wall where all CFD predictions still differ from the data.

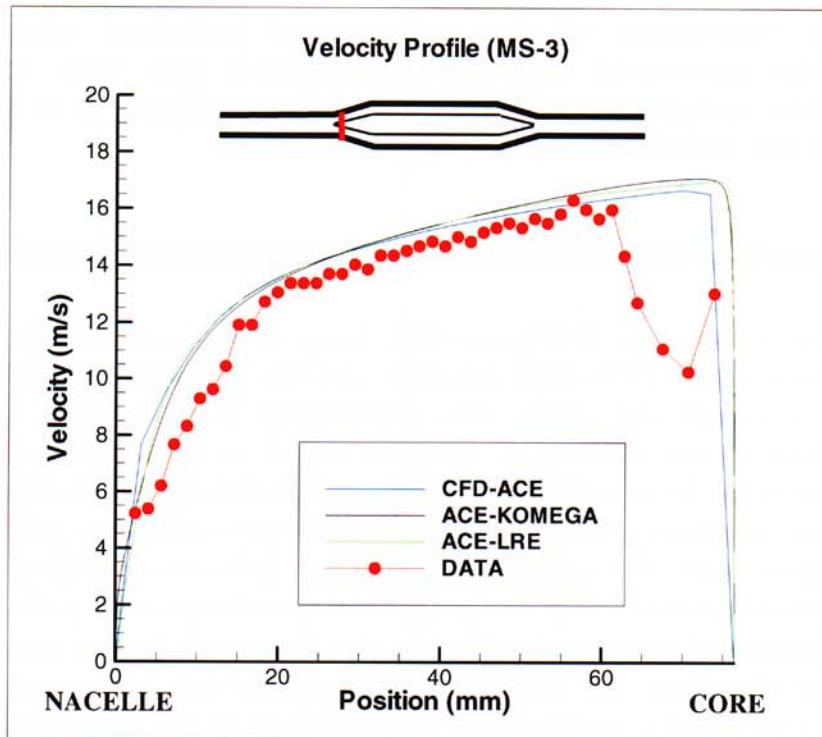


Figure 7.19 -  $k-\omega$  and Low Reynolds Results: Measurement Plane 3 Velocity Comparison

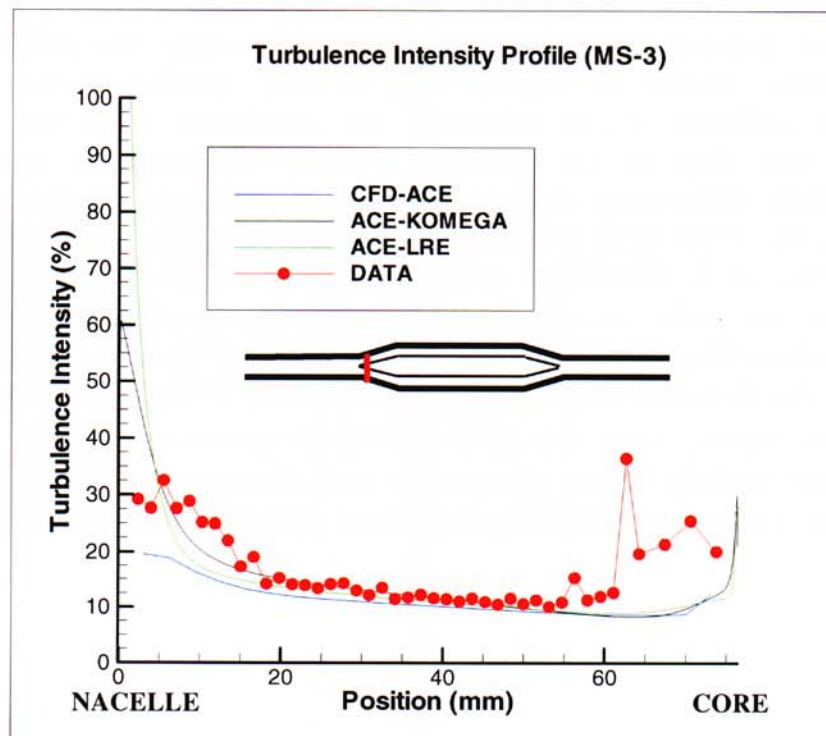


Figure 7.20 -  $k-\omega$  and Low Reynolds Results: Measurement Plane 3 Turbulence Intensity Comparison

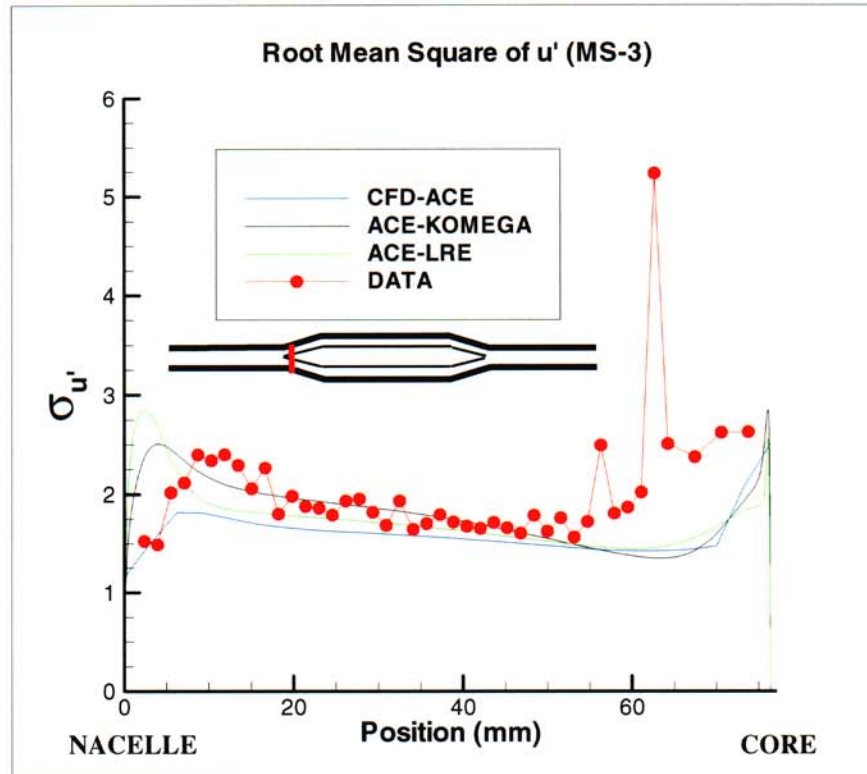


Figure 7.21 -  $k-\omega$  and Low Reynolds Results: Measurement Plane 3 Root Mean Square of  $u'_s$  Comparison

Overall, the use of wall functions did not severely impact the solution for this type of application. For this reason, it is even more likely that a small misalignment between the core and the flow direction caused the velocity dip near the core wall at measurement location 3.



## 8. Summary

Numerical simulations of air flow through a quarter-scale smooth nacelle geometry were performed using the VULCAN code and the CFD-ACE code. Comparisons of the numerical predictions with the experimental data from the 46 TW Aerospace Survivability and Safety Flight at WPAFB were performed in order to benchmark the CFD codes for this application. In general, the velocity predictions showed good agreement with the data in the center of the channel throughout the entire geometry but deviated near the walls. The turbulence intensity predictions also showed good agreement along the inlet section and at the start of the inlet transition duct section. The numerical predictions showed much larger turbulence intensity values in most of the inlet transition duct section and at the start of the straight annular section. These differences between the predictions and the experimental data were significantly affected by differences in mean velocity values, since mean velocity was used to normalize the turbulence intensity. When the rms values of the fluctuating streamwise velocity were plotted, the CFD predictions showed much better agreement with the experimental data. At the remaining downstream measurement planes, the data consistently showed larger turbulence intensity values, although the trends were similar. Some differences were observed between VULCAN and CFD-ACE results due to the cartesian grid structure used by the VULCAN code. These differences mainly occurred in the inlet transition duct and the outlet transition duct where the walls are angled. Also, the experimental data tended to show poorer resolution (higher measurement uncertainty) near the walls of the transition ducts. This occurrence may be due to the low signal to noise ratio as affected by wall curvature. In addition, it is also possible that a small misalignment between the core and the flow direction occurred in the experiment. A misalignment could explain some of the differences between the CFD predictions and the experimental data, especially in the inlet transition duct section.

In addition to the above comparisons, sensitivity studies were also performed using CFD-ACE in order to assess the effect of grid resolution, turbulence models, and wall functions on the results. First, a calculation was performed using a coarse mesh (factor of 7.7 less grid points). Overall, the coarse mesh solution showed good agreement with the fine mesh solution; differences were only observed near the walls due to the lack of grid resolution. A second CFD-ACE calculation was also performed to assess the effect of the turbulence model relation on the predicted results. In the original calculation, zero cross-stream turbulent velocities were assumed and in the second turbulent calculation, an isotropic turbulent flow assumption was used. Overall, the assumption of zero cross-stream turbulent velocities produced results in

better agreement with the experimental data than the isotropic turbulent flow assumption. Therefore, for this problem, the zero cross-stream turbulent velocity assumption is better than the isotropic turbulent flow assumption. This conclusion also agrees with experimental observations. Finally, both a  $k-\omega$  model calculation and a Low Reynolds Number  $k-\epsilon$  model calculation were performed to assess the effect of using wall functions. Small differences did result near the walls but the use of wall functions did not severely impact the numerical predictions for this application.

Overall, this effort provided a benchmark case for both the VULCAN and CFD-ACE codes for the application of interest. In addition, this study pointed out the importance of assessing the influence of the cross-stream velocities when calculating a turbulence intensity from a turbulent kinetic energy term. Also, the use of wall functions for this application was assessed and found to be adequate.



## References

1. Hamins, A., Cleary, T., Borthwick, P., Gorchkov, N., Mcgrattan, K., Forney, G., Grosshandler, W.L., Presser, C., and Melton, L., "Suppression in Engine Nacelle Fires, Section 9.4, Flow Field Modeling and Validation in a Mock Nacelle" in Fire Suppression System Performance of Alternative Agents in Aircraft Engine and Dry Bay Laboratory Simulations, NIST SP890, R.G. Gann, ed., pp. 84-104, 1995.
2. Wright Laboratory Technical Report WL-95-3077. Wright-Patterson AFB, Dayton, Ohio, 1995.
3. Wright Laboratory Technical Report WL-97-3076. Wright-Patterson AFB, Dayton, Ohio, 1997.
4. Lopez, A.R., Gritzo, L.A., and Hassan, B., "Computational Fluid Dynamics Simulation of the Air/Suppressant Flow in an Uncluttered F18 Engine Nacelle." Proceedings of the Halon Options Technical Working Conference, New Mexico Engineering Research Institute, Albuquerque, NM, pp. 281-297, 1997.
5. Holen, J., Brostrom, M., and Magnussen, B.F., "Finite Difference Calculation of Pool Fires." *The Twenty-Third Symposium (International) on Combustion*, The Combustion Institute, Pittsburgh, p. 1677-1683, 1990.
6. Magnussen, B.F., Hjertager, B.H., Olsen, J.G., and Bhaduri, D., "Effects of Turbulent Structure and Local Concentrations on Soot Formation and Combustion in C<sub>2</sub>H<sub>2</sub> Diffusion Flames." *The Seventeenth Symposium (International) on Combustion*, The Combustion Institute, Pittsburgh, p. 1383-1393, 1979.
7. Patankar, S.V., and Spalding, D.B., *Int. J. Heat Mass Transfer*, 15:1787, 1972.
8. CFD-GUI™, CFD-ACE Structured Flow Solver Manual, Version 5, CFD Research Corporation, Huntsville, Alabama, October, 1998.
9. CFD-ACE™, Theory Manual, Version 5, CFD Research Corporation, Huntsville, Alabama, October, 1998.
10. Launder, B. E. and Spalding, D. B., "The Numerical Calculation of Turbulent Flows", *Computational Methods Applied to Mechanics and Engineering*, 3, pp. 269-289, 1974.
11. Wilcox, D.C., "A Half Century Historical Review of the k- $\omega$  model," AIAA-91-0615, 1991.



12. Chien, T. and Smith, A.M.O., *Analysis of Turbulent Boundary Layers*, Academic Press, New York, 1982.
13. Bennett, J.M., Caggianelli, G.M., Kolleck, M.L., and Wheeler, J.A., "HALON REPLACEMENT PROGRAM FOR AVIATION Aircraft Engine Nacelle Application Phase I – Operational Parameters Study," WL-TR-95-3077, 1997.
14. Gridgen User Manual, Version 13, Pointwise, Inc., Bedford, Texas, 1998.
15. Disimile, P. and Tucker, J., Personal communication on the experimental results for tests conducted at Wright Patterson Air Force Base, 2001.
16. Libby, P. A. *Introduction to Turbulence*, Washington, D.C., p. 360, 1996.

## Distribution

Aerospace Survivability Flight (2)  
46OG/OGM/OL-AC  
Bldg. 1661B, Area B  
Attn: James R. Tucker  
WPAFB, OH 45433-7605

Mr. Andy Pascal  
P.O. Box 244  
Cedar Crest, NM 87008

Aerospace Survivability Flight  
Attn: Mr. Marty Lentz  
46OG/OGM/OL-AC  
Bldg. 1 Bldg. 1661B, Area B  
WPAFB, OH 45433-7605

INS Inc  
Attn: Dr. David Keyser  
Pinehill Technology Park,  
48015-A Pinehill Run Rd.  
Lexington Park, MD 20653

Aerospace Survivability Flight (2)  
Attn: Dr. Peter J. Disimile  
46OG/OGM/OL-AC  
Bldg. 1661B, Area B  
WPAFB, OH 45433-7605

NAWCWPNS  
Attn: Mr. Leo Budd  
Code 418300D  
1 Administration Circle  
China Lake, CA 93555-6100

National Institute of Standards and Technology (3)  
Attn: Dr. Richard Gann  
Building and Fire Research Laboratory  
100 Bureau Drive, Stop 8650  
Gaithersburg, MD 20899-8650

Naval Air Systems Command, AIR 4.3.5.1  
Aircraft Fire Protection  
Attn: Lawrence Ash  
48110 Shaw Rd., Bldg. 2187, Suite 3380-D4  
Patuxent River, MD 20670-5304

The Boeing Company – Phantom Works  
Attn: Glenn Harper  
Mailcode S106 7075  
PO Box 516  
St. Louis, MO 63166-0516

Air Force Aeronautical Systems Center  
Attn: Hugh Griffis  
Bldg. 11a, Room 101H  
1970 Monahan Way  
WPAFB, OH 45433-7208

### **Internal Distribution**

|    |         |       |  |
|----|---------|-------|--|
| 1  | MS 0841 | 09100 | T.C. Bickel                                    |
| 1  | MS 0847 | 09130 | J. L. Moya                                     |
| 1  | MS 0828 | 09133 | M. Pilch                                       |
| 10 | MS 0828 | 09133 | A. R. Black                                    |
| 5  | MS 1135 | 09132 | L. A. Gritz                                    |
| 1  | MS 0835 | 09111 | S. P. Domino                                   |
| 1  | MS 0825 | 09115 | C. J. Roy                                      |
| 1  | MS 1135 | 09132 | J. M. Nelson                                   |
| 1  | MS 1135 | 09132 | P. E. DesJardin                                |
| 1  | MS 1135 | 09132 | W. Gill  |
| 1  | MS 1135 | 09132 | V. F. Nicolette                                |
| 5  | MS 1135 | 09132 | J. M. Suo-Anttila                              |
| 1  | MS 1135 | 09132 | S. R. Tieszen                                  |
| 1  | MS 9042 | 08728 | C. D. Moen                                     |
| 1  | MS 9018 | 09018 | Central Technical Files, 8945-1                |
| 2  | MS 0899 | 00899 | Technical Library, 9616                        |
| 1  | MS 0612 | 00612 | Review and Approval Desk, 9612<br>For DOE/OSTI |



